

LUT UNIVERSITY  
LUT School of Energy Systems  
LUT Mechanical Engineering

*Mohammad Mizanur Rahman*

**HEAT AFFECTED ZONE STRESS-STRAIN RELATIONSHIP IN HIGH  
STRENGTH STEEL WELDS**

5.3.2022

Examiner(s): Professor Timo Björk  
D. Sc. (Tech.) Tuomas Skriko

## **ABSTRACT**

LUT University  
LUT School of Energy Systems  
LUT Mechanical Engineering

Mohammad Mizanur Rahman

### **Heat affected zone stress-strain relationship in high strength steel welds**

Master's thesis  
2022

64 pages, 48 figures, 14 table and 3 appendices

Examiners: Professor Timo Björk  
D. Sc. (Tech.) Tuomas Skriko

Keywords: S700, HAZ, high strength steel, HSS, welding, DIC, 3d optical measurement, ARAMIS, true stress – true strain, FEM.

The use of high-strength steel (HSS) has increased significantly in recent years and their weldability has improved considerably. HSS can improve the profitability of the production process and end product by reducing materials and allowing designers to use less and thinner material in a specific design. Despite these benefits, certain restrictions are preventing the utilization of higher steel grades in applications, since to date, there is no universal welding specification for HSS welds. This thesis aims to study mechanical properties (yield strength, tensile strength, elongation, etc.) of 4 mm thick SSAB's S700 steel weldments with two different heat inputs (0.38 kJ/mm and 0.68 kJ/mm). The local behavior of three different zones of weldments: base metal (BM), heat affected zone (HAZ), and weld metal (WM) was studied by conducting tensile tests and using digital image correlation (DIC) techniques.

Both tensile test and 3D optical measurement (ARAMIS) were done simultaneously. True strain data for different zones of the weldment was obtained directly from ARAMIS 3D optical strain measurements. Using this data, true stress - true strain curves of weldments for three different zones were plotted and proposed to be used in Finite Element Method (FEM) simulation. Test result data comparison between the universal tensile testing machine with extensometer and ARAMIS from base metal show similar mechanical properties, thus increasing the reliability of the results. The experimental results show that the strength of the weldments is lower than that of the base material and fracture was initiated at WM zone for low heat input and at HAZ for high heat input.

## ACKNOWLEDGEMENTS

This research has been done as a master's thesis in cooperation with LUT University and HAMK Tech, a research unit in Häme University of Applied Sciences (HAMK), in Finland. The research topic of this thesis is part of larger ongoing HSS welding research conducted in HAMK, supervised by the current research director Jarmo Havula. At first, I would like to thank research director Jarmo Havula and the personnel of HAMK Tech research unit for assisting me with the research work and laboratory tests. I would also like to thank Professor Timo Björk and head of welding technology at LUT, Tuomas Skriko, for supervising my thesis.

Last but not the least, I would like to thank my friends and family for supporting and encouraging me during my thesis work and studies.

*Mohammad Mizanur Rahman*

Mohammad Mizanur Rahman

Lappeenranta

5.3.2022

## LIST OF SYMBOLS AND ABBREVIATIONS

$c$	Specific heat [Jkg <sup>-1</sup> °C <sup>-1</sup> ]
$d$	Thickness [mm]
$E$	Young's modulus
$\varepsilon$	Thermal efficiency of the welding procedure
$\varepsilon_y$	Strain at yield
$\varepsilon_u$	Strain at tensile strength
$\varepsilon_T$	True strain
$f_u$	Tensile strength
$f_{u,BM}$	Tested base material (unwelded) tensile strength
$f_y$	Yield strength
$I$	Current [A]
$\rho$	Density [kgm <sup>-3</sup> ]
$Q$	Heat input
$T_0$	Initial temperature of the plate [°C]
$t_{8/5}$	Cooling time
$U$	Voltage [V]
$V$	Welding speed [mm/min]
$\lambda$	Thermal conductivity [Js <sup>-1</sup> m <sup>-1</sup> °C <sup>-1</sup> ]
BM	Base metal
DIC	Digital image correlation
EPS	Effective plastic strain
ES	Effective stress
FEM	Finite element method
GMAW	Gas metal arc welding
HAZ	Heat affected zone
HSS	High strength steel
MAG	Metal active gas
QT	Quenching and tempering
WPS	Welding procedure specification
WM	Weld metal

## TABLE OF CONTENTS

### ABSTRACT

### ACKNOWLEDGEMENTS

### LIST OF SYMBOLS AND ABBREVIATIONS

<b>1</b>	<b>INTRODUCTION .....</b>	<b>7</b>
1.1	Background information .....	7
1.2	Objectives and limitations .....	9
1.3	Research questions.....	10
<b>2</b>	<b>LITERATURE REVIEW .....</b>	<b>11</b>
2.1	Effects of heat input and cooling rate .....	11
2.2	Digital Image Correlation (DIC) technique to evaluate true stress-strain curves	13
<b>3</b>	<b>RESEARCH METHODOLOGY .....</b>	<b>18</b>
3.1	Overview of experimental research .....	18
3.2	Material used.....	18
3.3	Test samples.....	20
3.4	Welding process and parameters .....	22
3.4.1	Cooling rate measurements.....	24
3.5	Experiments and measurements.....	27
3.5.1	Tensile tests.....	27
3.5.2	Hardness tests .....	29
3.5.3	3D optical measurement process .....	29
<b>4</b>	<b>EXPERIMENTAL RESULTS AND ANALYSIS.....</b>	<b>33</b>
4.1	Tensile tests.....	33
4.2	Measurement of local tensile properties of weldments by using 3D optical measurement .....	37
4.3	True stress - true strain curve.....	42
4.4	Principle strain direction and rupture path.....	55
<b>5</b>	<b>DISCUSSION AND CONCLUSIONS.....</b>	<b>58</b>
<b>6</b>	<b>SUMMARY .....</b>	<b>60</b>
	<b>REFERENCES.....</b>	<b>61</b>
	<b>APPENDICES.....</b>	<b>1</b>

APPENDIX 1: Hardness test profile .....	1
APPENDIX 2: 3D scan data.....	3
APPENDIX 3: Major strain at different load stage .....	9

## 1 INTRODUCTION

This thesis investigates the stress-strain properties of welded S700 steels, especially heat-affected zones (HAZ) for different welding heat inputs and cooling times. In this work, HSS refers to steels with nominal yield strength from 500-1100 MPa (Keeler, Menachem, and Mooney, 2017, p. 29). The main welding process considered for producing the weld joints is gas metal arc welding (GMAW) also known as metal active gas (MAG) welding. The weld joints considered are single-V groove butt-welded joints.

High-strength steel became more popular in various structural applications for several reasons such as opportunities in weight reduction, higher load-carrying capacity, cost-effectiveness, etc (Hajro, 2017, p. 0611). The welded structure of high-strength steels can play an important role in the steel structure design process (Scholting and Weber, 2007, p. 122). Compared to the mid steel weldments, HSSs weldments have very good strength-weight ratio which contributes to a reduction in material consumption (Havula et al., 2018, pp. 523-537). Despite this, a welding procedure specification (WPS) for welding these HSSs has not yet been developed up to this date. This led to many restrictions on using high-strength steel welded joints in structures, as incorrect welding parameters could lead to a weakening in the weld joint, usually in the heat-affected zone (HAZ). This uncertainty of welding HSSs can be solved by having appropriate welding parameters and proving their performance through experimental tests. Measuring mechanical properties of weldments requires highly accurate techniques and equipment. Many approaches such as universal tensile tests, 3D Optical Measurements (ARAMIS), thermomechanically controlled tests (Gleeble), etc. can be utilized for observing the mechanical properties of HSSs weldments (Shamsuri and Darus, 2020; Oliwa, 2015, pp. 54-62).

### 1.1 Background information

Welding high-strength steel using MAG welding process is a fusion welding process forming weld bead between two parts. This fusion is caused by high heat which melts the parts and joins them. Due to this high heat and consumable welding filler metal, both base materials and weld bead undergo several microstructural changes that affect the strength of the weldments (Singh, 2012, pp. 47-49). The weld then cools down rapidly and this itself

also causes modification on the material properties of the weld. Any part of the parent material affected by the heat of the welding without melting the actual metal is considered as heat-affected zones (Bowditch, 2010, pp. 54-59). During the fusion welding process, the most critical area of the welded joint is heat-affected zones (HAZ) due to the risk of fracture initiation from this area (Pirinen, 2015, pp. 129-130). The main role of the welded structure is to transmit force between adjacent parts. This welded joint structure must have describable mechanical properties, required ultimate load capacity, and ductility especially. These characteristics are controlled by many factors, such as steel grades, types of welds, base material, heat input, cooling rate, etc. (Sefcikova, 2015, pp. 1-2). The mechanical properties of HAZ and weld zone may vary from base material properties which mainly depends on welding parameters such as current, voltage, welding process, welding speed, etc. Welding parameters directly affect the cooling times, therefore the cooling time itself affects the properties of the welded joint. For mild steel grades, cooling rates from 800 - 500°C do not cause a significant change in the microstructure of the steel. However, for steels with higher tensile strength than 500 MPa, the cooling time from 800 - 500°C can cause critical changes in the microstructure of the steel, while negatively affecting the properties of the weld joint (Arora, 2020, pp. 423-427). The microstructure of the heat-affected zones mainly depends on the welding heat input and cooling rates (Pirinen, 2015, pp. 129-130). To understand better how the heat due to the welding parameters has affected the weld and the HAZ, cooling time measurements may be taken during the welding or calculations may be conducted based on welding and joint parameters. By controlling heat input and cooling rate, it is possible to achieve the required mechanical properties of the weldments (Gourd, 1995). In the HSS welding process, fast cooling rates lead to a risk of microstructure hardening and further loss of cold crack resistance. However, in some direct-quenched steel grades, it is desirable to have low welding heat inputs and thus, rapid cooling rates. On the other hand, slow cooling rates lead to loss of toughness (Hajro, Hodzic and Tasic, 2017, p. 0611). Therefore, it is important for welding HSS to have recommended cooling rates guidelines. Cooling rate measurements would allow researchers to investigate relations between heat inputs and weld joint properties by varying appropriate welding parameters.

The mechanical properties (the ultimate strength, yield strength, elongation, nature of fracture, etc.) and fracture characteristics of welded structure can be observed through stress-strain characteristics. Transverse tensile test device and 3D Optical Measurement



(ARAMIS) were utilized in this study to observe stress-strain characteristics. ARAMIS is a measurement tool based on 3D scanning of the surface of the tested material (Walotek, Bzówka and Ciołczyk, 202, p. 4600). The stress-strain curve obtained from tensile diagram is called engineering stress-strain diagram where curve is generated based on original cross-section and gauge length. This process of stress-strain properties determination is good enough for many engineering problems if contradiction and plastic strains are not significant (Milošević et al., 2021, p. 4691). High-strength steel weldments requires more precise evaluation of stress-strain curve due to elastic-plastic tensile properties of various regions in weld joints. In that case, true stress-strain curve can precisely evaluate tensile properties of welded joints, especially heat affected zones (Milošević et al., 2021, p. 4691). Stier et al. (2011) mentioned that the 3D optical measurement approach is appropriate for understanding material behavior, especially at high strains.

## 1.2 Objectives and limitations

The purpose of this research is to develop true stress-strain curve of S700 weldments for three different zones (HAZ, BM, and WM) under various heat inputs and compare stress-strain curve of weldments with the base material stress-strain curve. This research contains laboratory experiments using digital image correlation (DIC) techniques (ARAMIS) and tensile tests with an extensometer as well as hardness measurement. Material heterogeneity effect on the behavior of weldments makes it difficult to analyze the mechanical properties of the welded structure. However, 3D Optical Measurement (ARAMIS) system can reveal the local behavior of the weldments, especially at the HAZ, during a tensile test. The obtained data from ARAMIS software can be used as material input data for finite element modelling programs (e.g. LS-Dyna). One example of material input data of LS-Dyna is shown in figure 1, where material properties such as effective plastic strain (EPS), effective stress (ES), etc. data are used as material properties.

Keyword Input Form

NewID  Use \*Parameter  Comment (Subsys: 1 Solid model run 17.5.k) Setting

\*MAT\_PIECEWISE\_LINEAR\_PLASTICITY\_(TITLE) (024) (3)

TITLE  
Base material S500

1	MID	RQ	E	PR	SIGY	ETAN	FAIL	TDEL
	1	7.800e-06	200.00000	0.3000000	0.5000000	0.0	0.4000000	0.0

2	C	P	LCSS	LCSR	VP
	0.0	0.0	0	0	0.0

3	EPS1	EPS2	EPS3	EPS4	EPS5	EPS6	EPS7	EPS8
	0.0	0.0047000	0.0072000	0.0169000	0.0268000	0.0367000	0.0467000	0.0548000

4	ES1	ES2	ES3	ES4	ES5	ES6	ES7	ES8
	0.5000000	0.5580000	0.5720000	0.6100000	0.6390000	0.6570000	0.6670000	0.6760000

Plot Raise New Padd

ES1:= Corresponding yield stress value to EPS1

1 Base material S500  
2 Filler material  
3 HAZ

Figure 1. Example of material input parameters of LS-Dyna (Ngo, 2021, p. 12).

### 1.3 Research questions

Finding suitable mechanical properties and fracture characteristics of HSS weldments by optimizing welding parameters will be a key issue in this research. Simulation of the welded joints with finite element modelling can predict precisely the behavior of HSS weldments. Correctly defined material properties of weldments for input data of the simulation process, is the main research problem in this master's thesis. Based on the research problem, following research questions derived and answered in this thesis:

- What are the mechanical properties in three different zones (HAZ, WM, and BM) of welded joint?
- What is true stress- true strain curve for welded joint in different zones.
- How different heat inputs effects the mechanical behavior of heat affected zones.
- How to utilize realistic estimation of the material properties to construct a correct finite element model (FEM).

Different approaches can be utilized in order to validate the research findings.

## 2 LITERATURE REVIEW

Due to HSSs very good strength-weight ratio, there is a reasonable motivation to research welding of these steels and investigate the weld joint's behavior. Many recent studies have been done and concluded that the properties of HSS welded joints will be compromised if inadequate welding parameters are used.

In different research works, several welding processes are studied to join high-strength steel. For example, Guo et al. (2015) conducted a study on laser welding process of S960 HSS and demonstrated that the laser welding process could display good tensile and bending properties. In another research, Guo et al. (2017) studied that the narrow gap laser welding joints can show better tensile properties than the gas metal arc welding (GMAW). In the study that is done by Lee et al. (2014), the microstructure characteristics and tensile properties of dual-phase steel (DP780) were investigated by using three methods of welding, which were laser welding, tungsten inert gas (TIG), and metal active gas (MAG) welding. In this study, it was found that the size of the weld zone depends on welding heat inputs. It also mentioned that with the increase of cooling rate, the hardness of the weld metal and HAZ increases (Lee et al., 2014). Amraei et al. (2019) utilize GMAW and laser welding process to investigate mechanical properties of S700, S960, and S1100 weldments and finds that the fracture happened at base metal for S700 and S1100 weldments and for S1100 fracture happened at heat affected zones, which reduces the joint's ductility and strength.

### 2.1 Effects of heat input and cooling rate

The heat-affected zone is the most critical during the fusion welding process as this region undergoes several microstructure changes (Kim, 2001). Heat affected zone is the region of the base metal influenced by the heat applied during the welding of the given metal system. The area of the heat-affected zone can be defined by the distance up to which the change in properties and microstructure of the base metal is observed, which depends on several factors such as base metal, welding process, heat input, and so on.

The joint's capacity, toughness, and ductility of the weldments are affected by the welding heat input and cooling rate (Farrokhi, Siltanen, and Salminen, 2015, pp. 9-15). The cooling rate of weld metal depends on several parameters. Among them, heat input is the most critical parameter. High-strength steel weldments are more prone to the adverse effects of heat input than the lower steel grades (Azhari, 2017; Amraei, Dabiri, Björk and Skriko, 2016, pp. 114-125). The welding heat input can seriously affect the mechanical toughness properties of HAZ and the weld metal itself.

In many cases, higher and lower welding heat input values can negatively affect weld joint mechanical properties. In general, if other affecting parameters are kept constant, the cooling rate of the weld metal decreases due to the increase of heat input (Ghazvinloo & Honarbakhsh-Raouf, 2020, p. 361). Higher heat input leads to excessive grain growth. On the other hand, lower heat input results in an unrefined grain structure and produces a higher yield and tensile strength weld deposit than base material strength. The heat input of the welding process is controlled by voltage, amperage, and travel speed along with process-dependent thermal efficiency. Using incorrect parameters such as excessive voltage can reduce the effective mechanical properties of weldment as this causes small amounts of alloy to be lost in the arc. Similarly, excessive travel speed can result in rapid solidification of the weld bead.

Amraei et al. (2019) studied that in the case of fully automated gas metal arc welding (GMAW) process of thin S700 and S1100 weldments, the fracture is initiated at the base materials for both high and low welding heat inputs (HI). Additionally, the ductility of the welded joint also highly depends on HI values over the range of 0.3-1.4 kJ/mm for each welding pass (Amraei, 2019, p. 1).

According to Pirinen et al. (2015), in arc welding of high-strength steels, the tensile strength of the welded structure mainly depends on the chemical composition of the weld, weld geometry, parent material, and cooling rate of the metal, especially in the HAZ. In this study Pirinen et al. (2015), determine the mechanical properties of welded joints in 8 mm thick HSSs. Pirinen et al. (2015) concluded that compared to the tensile strength of the welded joint having electrode wire which equals 67-68% of the strength of the parent material, the

tensile strength of high-strength steel weldments is more than 15% higher (Pirinen, 2015, pp. 130-132).

In the study conducted by Yasuyama et al. (2007), the yield strengths ranging from 270 MPa to 980 MPa were compared by utilizing three different welding processes: YAG laser, mash seam, and plasma arc methods. A tensile test device conducted the test in both parallel and perpendicular to the weld direction. It was observed that the elongation of the weldments decreased compared to the base material for HSSs weldments.

The strength of filler materials also influences the ultimate strength of the welded structure. Rasche and Kuhlmann et al. (2009) mentioned that the strength of the weld joint of HSS weldments can be increased by increasing the strength of filler material. Collin et al. (2009) studied that it is possible to achieve base material strength using under-matched filler material test specimens. Khurshid et al. (2012) studied the effect of strength mismatch in weld metal and penetration ratio on HSS fillet welds' mechanical properties. This research asserted that under-matched filler materials are more sensitive to penetration ratio. It is possible to achieve parent material strength if the weld joint is fully penetrated with under-matched filler material (Khurshid, Barsoum and Mumtaz, 2012, pp. 36-42).

## 2.2 Digital Image Correlation (DIC) technique to evaluate true stress-strain curves

Because of material heterogeneity in weld zones, it is challenging to evaluate stress-strain properties (curves) precisely in different weld zones. Engineering stress-strain curves cannot predict accurately the material behavior of the ductile material beyond the ultimate stress (Younise, 2020, p. 5). Additionally, determining the mechanical properties of weldment regions may be difficult for the transversally applied load. Younise et al (2020), mentioned that combined experimental and numerical processes using power-law numerical equations can estimate mechanical properties of various regions of a weldment. Younise et al (2020) used DIC measurement was utilized as the initial reference point for numerical simulation (ABAQUS). Many researchers recommended new approaches for strain measurement, such as digital image correlation (DIC) method. DIC is a precise non-contact measuring system to measure the displacement and strain of a structure subjected to external load. (Milosevic, 2021, p. 43; Jovicic, 2017, pp. 28-42.)

Younisea et al. (2020) researched to estimate true stress-strain curves for High strength low alloy (HSLA) steel weldment by using iteration process based on DIC and FEM simulation. The power-law relation was utilized for a good approximation of stress-strain curves using combined experimental and numerical processes. In the study of Younisea, both tensile tests and 3D Optical Measurement (ARAMIS) were done simultaneously. Through ARAMIS software engineering remote stress - true strain data was obtained for different welded joint regions (base material, HAZ, and weld metal), shown in figure 3. Strains in each region for different loads were recorded by averaging strains along measured section lengths, shown in figure 2.

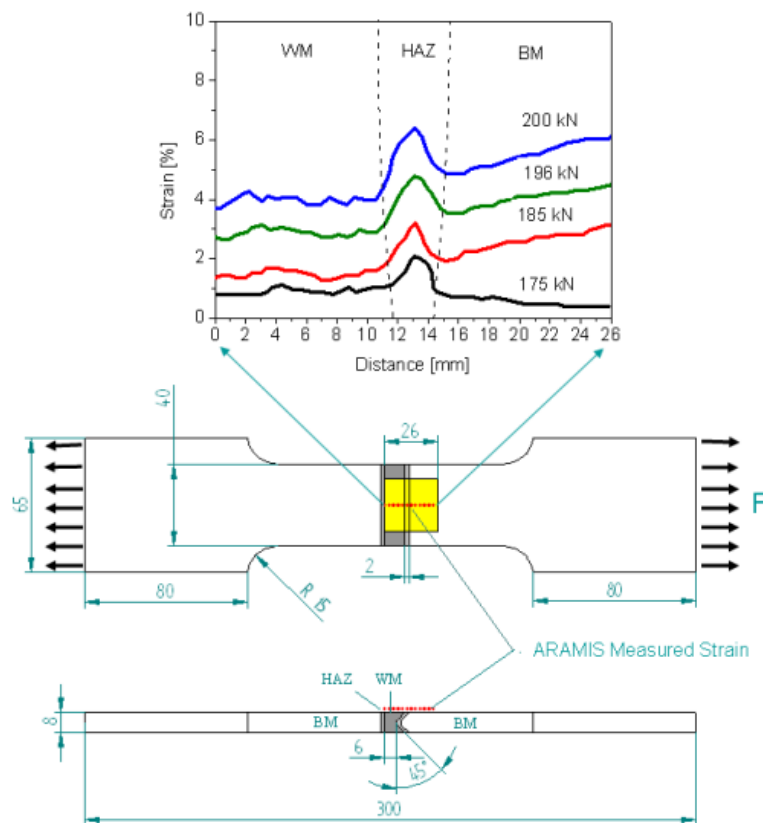


Figure 2. ARAMIS measure strain at various loads (Younisea, 2020, p. 5).

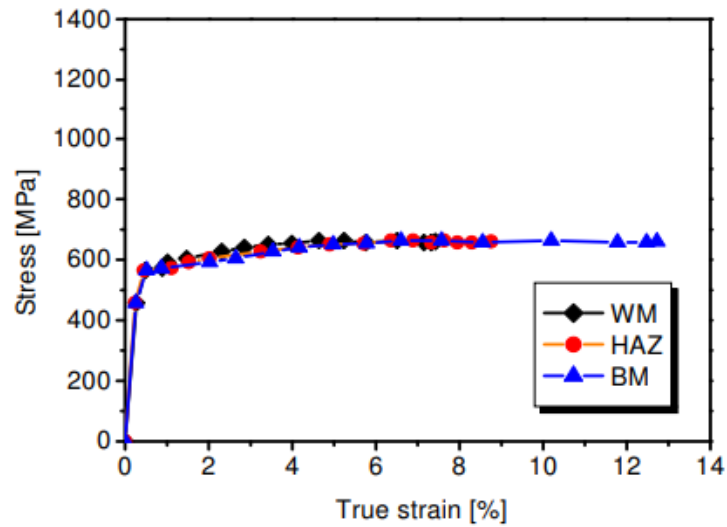


Figure 3. Engineering remote stress – true strain data from ARAMIS software (Younisea, 2020, p. 5).

Younisea et al. converted engineering remote stress ( $\sigma$ ) to true stress ( $\sigma_T$ ) using the formula:  $\sigma_T = \sigma(1 + \varepsilon)$ , where  $\varepsilon$  is the true strain (Ling, 1996). Calculated true stress-strain curves were used as the initial iteration for the FEM simulator (ABAQUS) using Hollomon power law (shown in figure 4). This research concluded that the iterative method of matching experimental and numerical analysis effectively estimates true stress-strain curves for different weld zones.

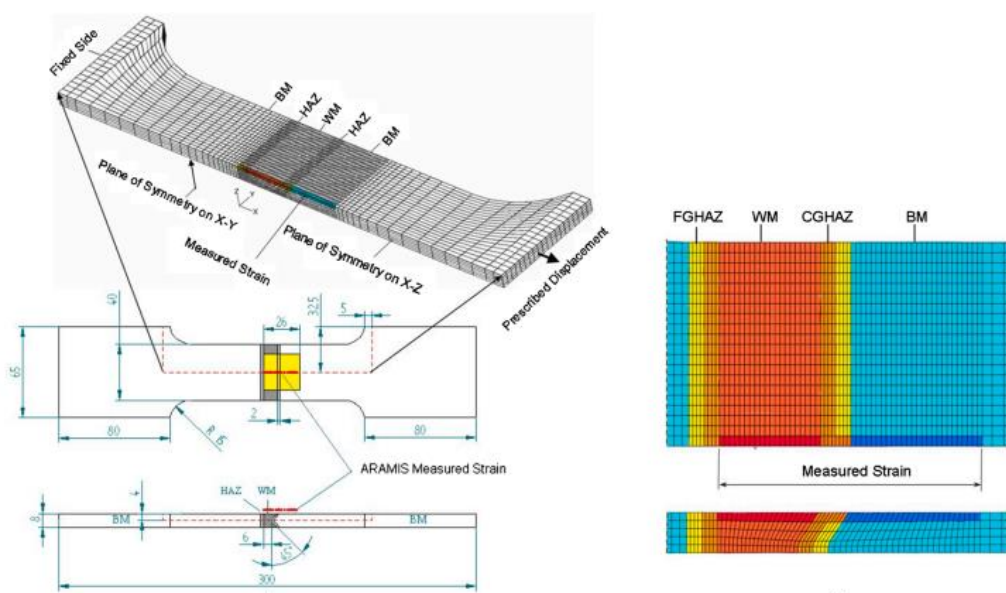
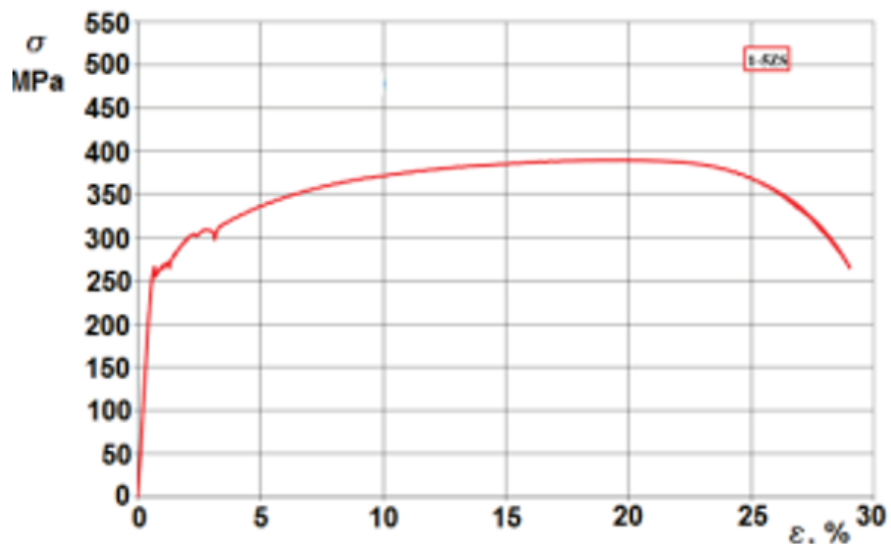


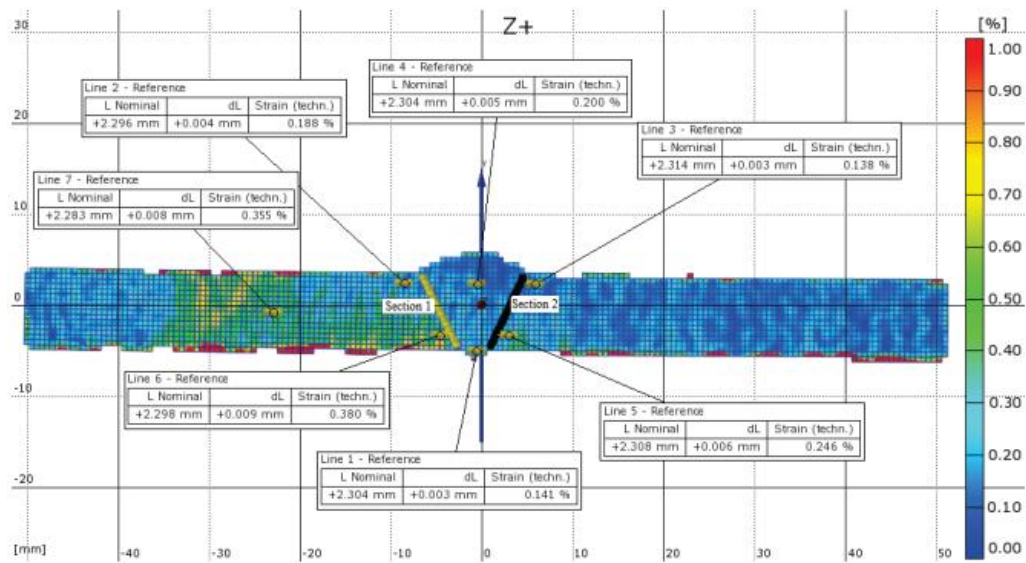
Figure 4. FEM mesh analysis by using ARAMIS measured strains for selected regions (Younisea, 2020, p. 6).

Milosevic et al. (2016), studied stiffness in local zones of weldment by using a digital image correlation (ARAMIS) system. This research paper presented the application of the DIC method utilizing ARAMIS software for analyzing local displacement and strain in a welded joint. The experiment was conducted using DIC system (ARAMIS) and a universal tensile testing device. Stress-strain diagram were obtained directly from the tensile testing device. Through ARAMIS software, strain was obtained by using a tool called “point-point” distance, shown in figure 5. Then, both results were compared to calculate stiffness (curve) in weld zones. It can be observed from figure 5 that the highest strain occurs in the BM and root side of the HAZ, values are 0.6 % to 0.7 %, which compiles the strain values recorded from the tensile testing device at yield limit (0.67 %) (Milosevic, 2016, p. 29).



a)





b)

Figure 5. a) Stress-strain curve obtained directly from tensile testing device. b) Strain at yield point (ARAMIS) (Milosevic, 2016, p. 11).

In another research which is commissioned by HAMK Tech, a research unit in Häme University of Applied Sciences, LS-Dyna software was utilized for analyzing finite element model (FEM) of three different zones of a weldment. Base material and filler material properties can obtain from LS-Dyna software as it has a wide range of available options roughly 300 material input data (Ngo, 2021, p. 5).

### 3 RESEARCH METHODOLOGY

This section describes the work methods, equipment, and tools used in this research work. It also describes the parameters used in the welding process.

#### 3.1 Overview of experimental research

In this work, the weld joints chosen are butt-welded joints, which were also compared to Gleeble simulated specimens. Plates with 4 mm thickness were welded with GMAW/MAG welding process. To investigate the effect of the welding parameters, real-time cooling rate values were recorded during welding process. Preliminary welding in the HAMK laboratory were done first to test the whole test arrangement (tensile tests with extension meter and ARAMIS system). Then, all tensile test specimens were water cut in required shape. For precise heat treatment and more controlled cooling times  $t_{8/5}$  to achieve HAZ properties, Gleeble thermomechanical simulator can be utilized in future research work. For this reason, two different sizes of specimens: 1) large size (LS) 2) small (Gleeble) size (SS) were tested in this research work. Then, obtained results were compared with base material samples tested results.

From the tensile tests using the extension meter and the ARAMIS system, true stress-strain curve can be found. Engineering stress-strain curves were developed for samples with different cooling times by using extension meter. The idea here is to develop an assumption of how different cooling times would affect the stress-strain curve. Similar tests are then conducted with base material S700 to find and compare the stress-strain curves between the weldments and base metal samples.

#### 3.2 Material used

Strenx 700 MC PLUS manufactured by SSAB was used as the material to be welded in this work. This steel has high-strength properties with advanced cold formability and impact toughness with a minimum yield strength of 700 MPa (SSAB, 2021). The mechanical properties given by the manufacturer are shown in table 1. The impact strength properties

are shown in table 2. Table 3 includes the chemical composition, and the carbon equivalent values are shown in table 4.

*Table 1. Mechanical properties of Strenx 700 MC PLUS (SSAB, 2021).*

Thickness	Yield strength $R_{eH}$ (min)	Tensile strength ( $R_m$ )	Elongation $A_5$ (min)	Min. inner bending radius for 90° bend
[mm]	[MPa]	[MPa]	[%]	[mm]
3.0 – 10.0	700	750-950	13	1.0 x t
10.01-12	700	750-950	13	1.5 x t

*Table 2. Impact strength properties of Strenx 700MC Plus (SSAB, 2021).*

Test direction	Min. impact energy for Charpy V 10x10 mm tests specimens
Longitudinal	40 J/ -40 °C

*Table 3. Chemical composition of Strenx 700MC PLUS (SSAB, 2021).*

C (max)	Si (max)	Mn (max)	P (max)	S (max)	Al (min)
[%]	[%]	[%]	[%]	[%]	[%]
0.12	0.25	2.10	0.020	0.010	0.015

*Table 4. Carbon equivalent CET (CEV) (SSAB, 2021).*

Thickness	Typical CET
[mm]	(CEV)
3.0 – 8.0	0.24 (0.338)
11.5-12.0	0.26 (0.40)

The filler material used for the welds was Ceweld ER 120 S-G with classifications according to EN ISO 16834-A. This material has high mechanical properties and excellent welding characteristics (CEWELD, 2021). Its mechanical properties are shown in table 5. The filler wire's chemical composition is shown in table 6.

Table 5. Mechanical properties of the filler wire (CEWELD, 2021).

Wire diameter	Yield strength $R_{p0.2}$	Tensile strength $R_m$	Elongation $A_5 (L_0 = 5d_0)$	Impact energy ISO-V KV	Impact energy ISO-V KV
[mm]	[MPa]	[MPa]	[%]	J	J
1.0	>690	>800	>19	>100 J/ -20 °C	>47 J/ -60 °C

Table 6. Chemical composition of the filler wire (CEWELD, 2021).

C	Si	Mn	Cr	Mo	Ni
[%]	[%]	[%]	[%]	[%]	[%]
0.08	0.6	1.60	0.30	0.30	1.50

### 3.3 Test samples

The welded samples considered in this work were butt-welded joints. Two types of heat inputs (HI): high and low were applied in the welding process. For each heat input, three large size and three small size welded samples were tested. Therefore, a total of 12 welded samples were tested. Small size specimens were tested for future comparisons with Gleeble thermomechanical simulator. For comparing tensile properties of welded samples to the base metal properties, an additional of large size and small size base material samples (without welds) were tested. Table 7 shows all the test specimens.

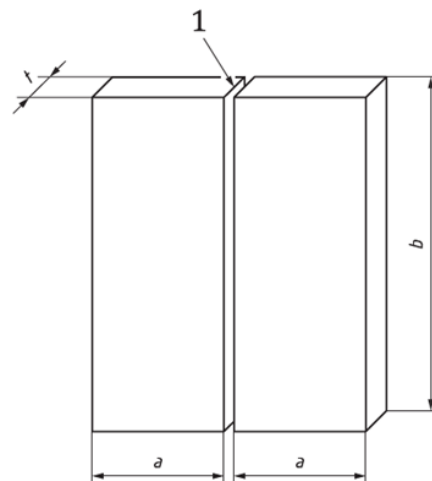
Table 7. Samples

#	Large plate names <sup>1)</sup>	Sample name	Heat input (kJ/mm)	Size of specimen	Gauge length*	
1	LS-Low HI	LS-1-Low HI	0.38	Shown in Figure 7	50 mm	
2		LS-2-Low HI				
3		LS-3-Low HI				
4	SS-Low HI	SS-1-Low HI		Shown in Figure 8		
5		SS-2-Low HI				
6		SS-3-Low HI				
7	LS-Low HI	LS-1-High HI	0.68	Shown in Figure 7	50 mm	
8		LS-2- High HI				
9		LS-3- High HI				
10	SS-Low HI	SS-1-High HI		Shown in Figure 8		20 mm
11		SS-2-High HI				

12		SS-3-High HI			
13	LS-Base		NA (no welds)	Shown in Figure 7	50 mm
14	SS-Base			Shown in Figure 8	20 mm

<sup>1)</sup> Large plates were welded as shown in Figure 6. After welding, tensile test samples were cut from the large welded plates.

Prior to welding, plates were cut from large sheets and then the edge of each plate was water cut for welding groove preparation (see figure 6) (SFS-EN ISO 15614-1:2017, 2017). Waterjet cutting machine was used, to ensure that no heat treatment occurs during the cutting of the samples. After samples were welded, they were water cut once more to the required geometry of tensile test specimens (shown in figure 7 and figure 8).



**Key**

- 1 joint preparation and fit-up as detailed in the preliminary welding procedure specification (pWPS)
- a* minimum dimension 150 mm
- b* minimum dimension 350 mm
- t* material thickness

Figure 6. Size of the test samples required for butt-weld joints with full penetration (SFS-EN ISO 15614-1:2017, 2017).

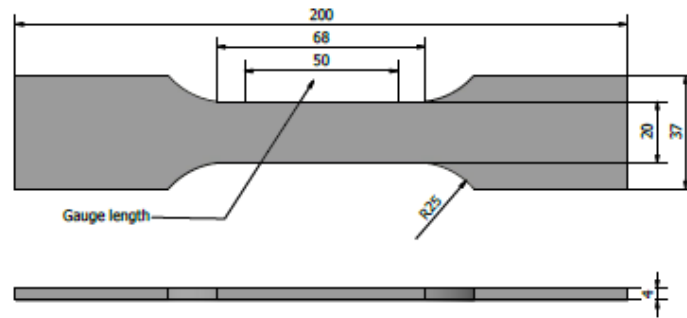


Figure 7. Tensile test specimen geometry for large size samples (LS series)

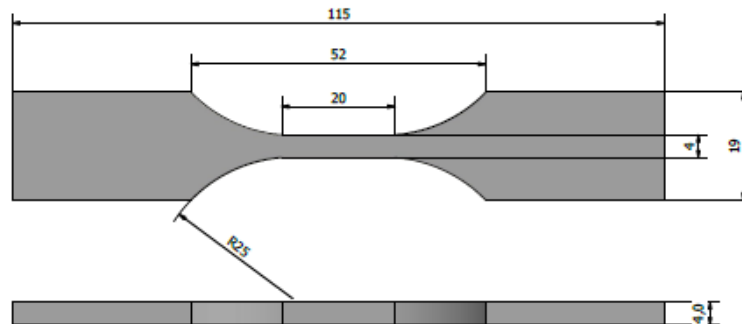


Figure 8. Tensile test specimen geometry for small size samples (SS series)

### 3.4 Welding process and parameters

Steel plates with grade Strenx 700 MC PLUS with thickness of 4 mm were chosen to be welded using the MAG welding process, with a butt-weld joint geometry (see Figure 9). The weld groove was prepared at an angle of  $60^\circ$  through a machining process to form a single-V butt joint.

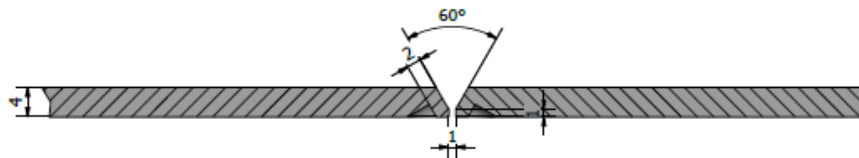


Figure 9. Size of plates for butt-welded joints and groove geometry.

The welding process was performed using a robotized system to achieve high-quality welding. Kemppi's FastMig WFX 300 welding machine was used to produce the weld. The welding device and setup are shown in figure 10.

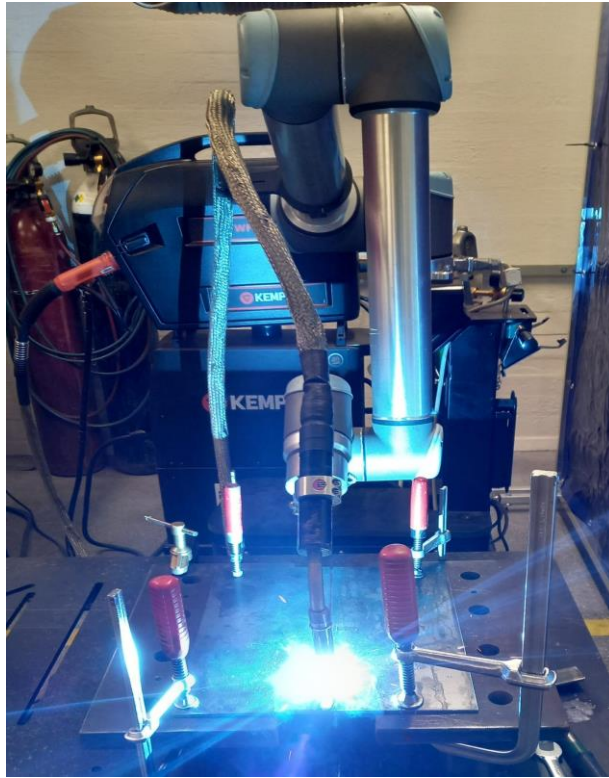


Figure 10. Welding setup.

The shielding gas used was Mison 18 which has a mixture of 18% CO<sub>2</sub> and 82% Argon. The welding parameters chosen are shown in Table 8.

Table 8. Welding parameters used.

#	Sample name	Heat input	Current	Voltage	Travel speed	Measured cooling time	Calculated 2D cooling time	Remarks
		(kJ/mm)	A	V	mm/s	s	s	
1	LS-1-Low HI	0.38	117	18	4.5	9.98	13.11	Cutting directions parallel to the rolling direction.
2	LS-2-Low HI							
3	LS-3-Low HI							
4	SS-1-Low HI							
5	SS-2-Low HI							
6	SS-3-Low HI							
7	LS-1-High HI	0.68	146	19.8	3.5	33.42	33.01	
8	LS-2-High HI							
9	LS-3-High HI							
10	SS-1-High HI							
11	SS-2-High HI							
12	SS-3-High HI							

Welding inspection was done visually according to the weld quality standard SFS-EN ISO 5817. Visual inspection was carried out in three phases: at the joint preparation, during the welding process, and after the welding is completed. Condition of the welded parts was checked as well as the depth/shape of the root penetration.

#### 3.4.1 Cooling rate measurements

To investigate the effect of the welding parameters on the welded joint, real-time cooling rate measurements were conducted during the welding, on the weld samples. The cooling time from 800°C to 500°C (known as  $t_{8/5}$  time) is of great importance, as this represents the range of temperature during which critical change occurs in the microstructure of the steel (Nejković, 2019). Thermocouples, an infrared camera, or a pyrometer, can then be used to measure the cooling rate from the weld samples. The three options can also be used in combination with one another to validate and compare the results. For monitoring the temperature changes during the welding process, two thermocouple holes were placed vertically in the direction of the 60-degree angle next to the heat-affected zone in the welded specimen.

In this study, K-type thermocouple was used for determining cooling rates. These thermocouples can measure temperatures up to 1260°C. An example of a welding setup where thermocouples are used to record temperatures without probes can be seen in Figure 11.



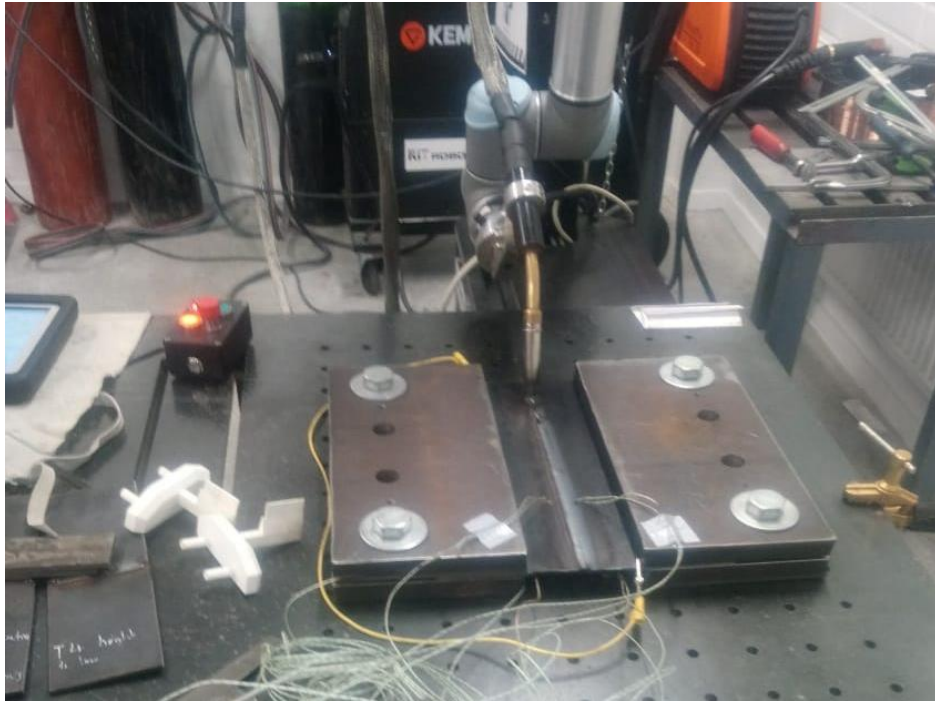


Figure 11. Example of a welding setup with the thermocouples installed in the plates without probes.

The cooling time can also be calculated as specified in EN 1011-2 (EN 1011-2 D4, 2001). Several equations are given depending on the heat flow and the dependency of the thickness on the cooling time. It must be noted however that some research has shown that the equations below may lead to errors when evaluating cooling time  $t_{8/5}$  and proposals to correct the formulas were given (Nejković, 2019, pp. 3975-3984). The EN 1011-2 has not yet released an update in response to this and other research.

For general cases with three-dimensional heat flow and cooling time being independent from material thickness, following equation determine the cooling time  $t_{8/5}$ .

$$t_{8/5} = \frac{Q}{2\pi\lambda} \times \left( \frac{1}{500-T_0} - \frac{1}{800-T_0} \right) \quad (1)$$

With three-dimensional heat flow cases and if material belongs to unalloyed and low alloyed steel, the equation is updated to include shape factors as well (given in Figure 16), and following equation can be used.

$$t_{8/5} = (6700 - 5T_0) \times Q \times \left( \frac{1}{500-T_0} - \frac{1}{800-T_0} \right) \times F_3 \quad (2)$$

Generally, when the heat flow is two-dimensional and material thickness plays a role in cooling time. Following equation can be used for determining cooling time  $t_{8/5}$ .

$$t_{8/5} = \frac{Q^2}{4\pi\lambda\rho cd^2} \times \left( \frac{1}{(500-T_0)^2} - \frac{1}{(800-T_0)^2} \right) \quad (3)$$

Equation (3) can be used for determining cooling time  $t_{8/5}$ .

$$t_{8/5} = (4300 - 4,3T_0) \times 10^5 \times \frac{Q^2}{d^2} \times \left( \left( \frac{1}{500-T_0} \right)^2 - \left( \frac{1}{800-T_0} \right)^2 \right) \times F_2 \quad (4)$$

For two-dimensional heat flow cases for unalloyed and low-allowed steels, the equation (4) is given, for calculating cooling time  $t_{8/5}$ .

Where:

Q stands for heat input,

$\lambda$  is the thermal conductivity [ $\text{Js}^{-1}\text{m}^{-1}\text{°C}^{-1}$ ]

$\rho$  is the density [ $\text{kgm}^{-3}$ ],

c is the specific heat [ $\text{Jkg}^{-1}\text{°C}^{-1}$ ],

d is the thickness

$T_0$  is the initial temperature of the plate [ $\text{°C}$ ]

$F_2$  and  $F_3$  are joint shape coefficients.

The heat input Q can be calculated from following equation.

$$Q = \varepsilon \cdot \frac{60 \cdot U \cdot I}{1000 \cdot V} \quad (5)$$

where:

$\varepsilon$  is the thermal efficiency of the welding procedure,

U is the voltage [V],

I is the current [A]

V is the welding speed [mm/min].

### 3.5 Experiments and measurements

This section contains experimental procedures, experiment setup, and the principle of experimental devices. In this research, tensile test with extensometer and 3D optical measurement were performed simultaneously.

#### 3.5.1 Tensile tests

Standard quasi-static tensile tests were performed on a Zwick / Roell 2500KN tensile test machine with an extension meter. The test was carried out according to the test standard DIN EN ISO 6892-1. The tensile test samples were prepared according to standard EN ISO 15614\_1:2017. The original gauge length of the specimen is 50 mm and the thickness is 4 mm. The dimension of the tensile test samples is shown in figure 7 and figure 8.

The testing device consists of a test frame that is equipped with testing software, crossheads, clamping jaws, load cell, and accessories, such as extensometers. The tensile test is performed by attaching the specimen (shown in Figure 12) to the pulling device with the clamping jaws at the top and bottom crosshead. The dimensions of the specimen are measured before the test (thickness, width, total length, gauge length). Then all the measured data are stored in the program software. All necessary testing parameters are selected on the control computer. Through the software, a command is given to the device. The pulling device then applies a continuously increasing tensile load to the specimen. The increase in load is continued until the specimen breaks.



Figure 12. Tensile test setup.

The load and the displacement were recorded to obtain the tensile strength at the yielding point and the maximum tensile strength as well as the elongation of the specimen. The mechanical properties of the specimen were observed in a force elongation diagram.

### 3.5.2 Hardness tests

In the hardness test, a cross section of the welded part is required for the examination. The cutting of cross section should be performed mechanically so that it does not affect the hardness values obtained. The cross-section should be sanded, polished and etched so that measurements can be made accurately in different parts of the weld zones. The hardness of the specimen is measured using Innovatest automated hardness tester which is set for Vickers hardness test. The hardness of specimen is taken from different points next to each other, on the same line, shown in appendix 1. The data obtained from each press is retrieved and formed into a cross-section hardness profile.

### 3.5.3 3D optical measurement process

The ARAMIS is a measurement tool based on 3D scanning of the surface of the tested material (Walotek, Bzówka and Ciołczyk, 2021, p. 4600). This device takes a series of time-lapse images of the measuring objects under investigation. The software tracks and identifies points on the surface of the testing specimen by taking images using common focal length. The points are identified in each stage and their positions are measured with subpixel accuracy. In this way, 3D model of the specimen can be built. The ARAMIS software can measure the displacement, velocity, shear angle, and accelerations caused by the external force from this 3D model. This device consists of special sets of stereo cameras and lenses, a power control, and Aramis software, shown in Figure 13.

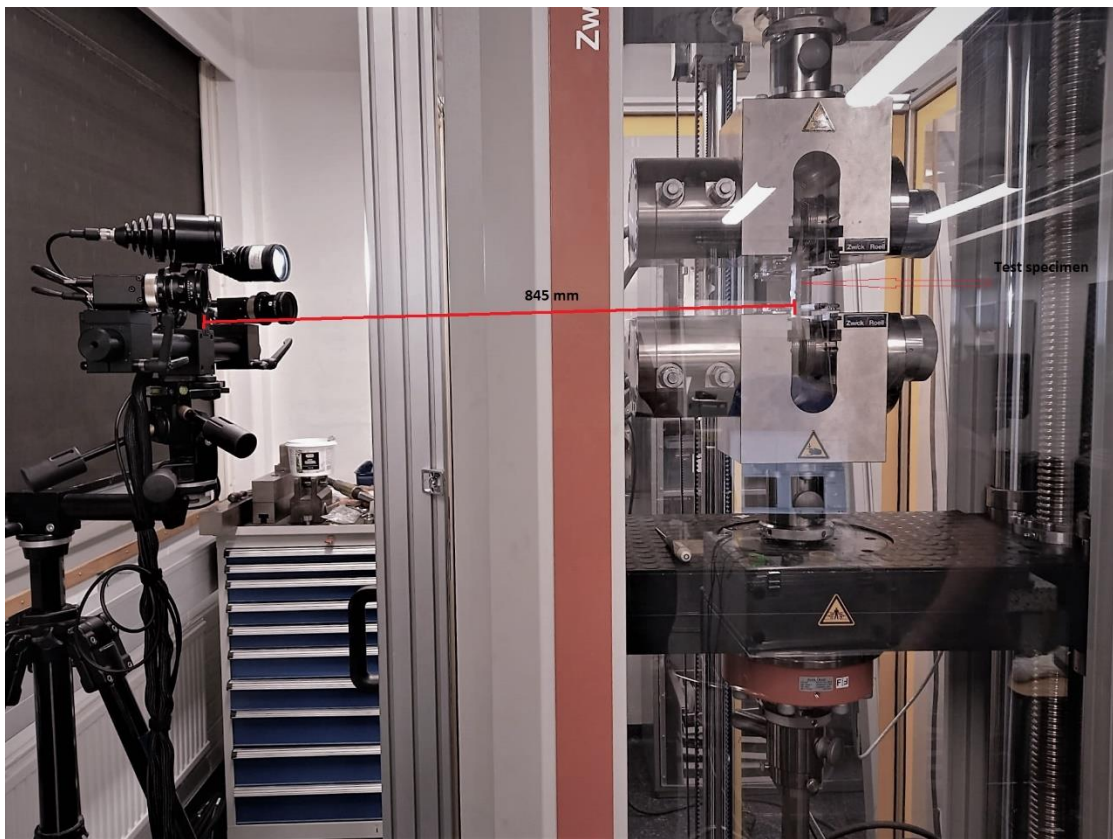


Figure 13. 3D optical measurement (Aramis) setup.

At the beginning of the test, the pace of the test is short. Therefore, faster imaging acquisition for example 10 frames per second required to evaluate the Young's Modulus and the Poisson Ratio very well. Slower imaging acquisition can be carried out after the transition from elastic to plastic deformation. However, in this experiment same imaging acquisition is carried out which is 10 frames per second.

Prior to the actual test, the calibration process was performed using calibration panels shown in figure 14. Different calibration panels can be used for different measurement volumes. Based on the ARAMIS instruction manual, the chosen measuring volume for this experiment was (125 X 100). The calibration process was successfully done by the alignment of the measurement volume and the camera position. For correct calibration, the calibration deviation should be in the range between 0.01 to 0.04 pixels (Milosevic and Mitrovic, 2011, pp. 112-115). The obtained calibration deviation was 0.038 pixels. Figure 14 shows different calibration panels and cross.

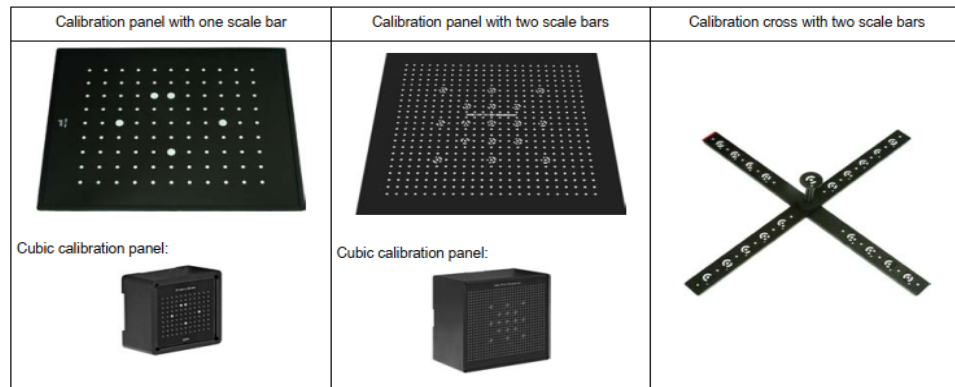


Figure 14. Calibration panels and cross (ARAMIS user manual, 2009, p. 8).

As the specimen is subject to loading, pretreatment to the surface of the specimen is necessary. The specimens which are placed in the tensile test must be marked with referral points. So that referral points can adhere to the surface and create the best possible contrast. Therefore, before applying the stochastic pattern, the specimens were kept in the acid solution for 24 hours so that paint can adhere to the surface of the specimen. Figure 15 shows the best possible stochastic patterns. Based on this example stochastic pattern was applied in all test samples, shown in figure 16.

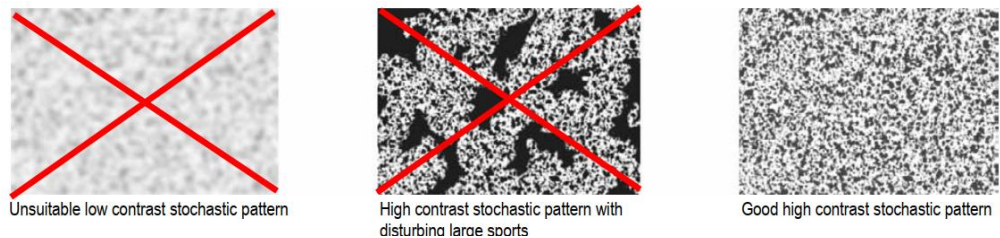


Figure 15. Example of a suitable stochastic pattern (ARAMIS user manual, 2009. P. 9).

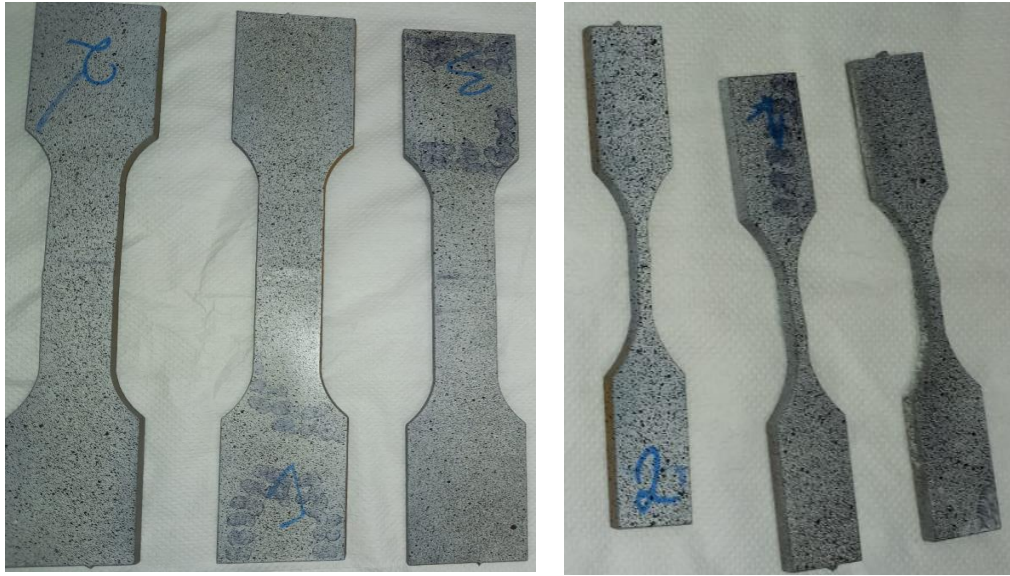


Figure 16. Stochastic pattern applied to the test specimen before tensile test.

The test and measurement process can start after completing the calibration process successfully. This process includes creating a new project, triggering types, setting the recording speed, and lighting around the specimen. The software starts to capture the images in various load stages after pressing the start triggering button. Then the next step is to define the evaluating area and a start point. Finally, Aramis software is ready to do the computation process. During computation, the software observes the images through various facets. (Mitrovic, 2011, p. 58)



## 4 EXPERIMENTAL RESULTS AND ANALYSIS

Tensile tests were conducted on all samples until failure occurred. Both tensile tests and 3D optical measurement processes were carried out simultaneously. As welded samples undergo different heat treatment process, tensile test (using extensometer) results cannot predict the local behavior of a welded structure, specifically HAZ. In this research, 3D optical measurement (ARAMIS) system was utilized to obtain true strain data for different weld zones. Engineering stress data was obtained directly from tensile testing device. After that, by converting engineering stress to true stress, true stress – true strain curves were plotted. As mentioned in chapter 3, in this experiment two types of samples were tested. The gauge length of the small size samples was 20 mm and for large size, the length was 50 mm. 3D scan was carried out before actual test to measure the actual cross section area at breaking point of the sample (shown in appendix 2). For low HI welded samples, the cross-section area at weld metal zone reduces, due to low deposit of weld metal, shown in appendix 1.

### 4.1 Tensile tests

All the representative engineering stress-strain curves of large size (LS) and small size (SS) welded samples with two different heat inputs (0.38 kJ/mm and 0.68 kJ/mm) are plotted in figure 17 (High HI), 18 (Low HI) and figure 20 (High HI), 21(Low HI) respectively. The average data of the three samples cut from the same large welded plate are compared with base material samples by plotting the stress-strain curve (shown in figure 19 and 22). Similarly, all the reduced mechanical properties of the welded samples are summarized in table 9 (large sample) and table 10 (small sample) together with base material samples mechanical properties for comparison.

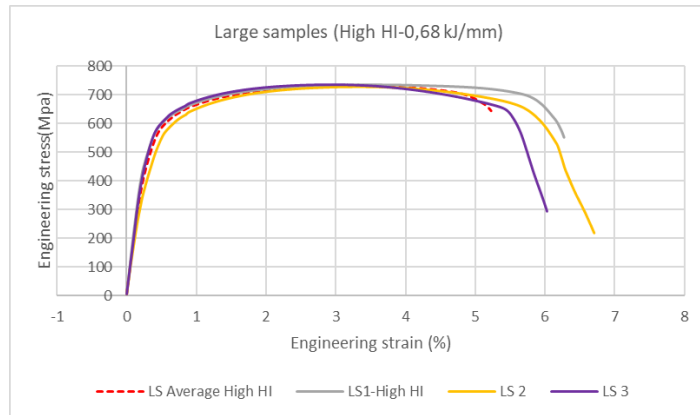


Figure 17. Engineering stress – engineering strain for large size samples (High HI-LS)

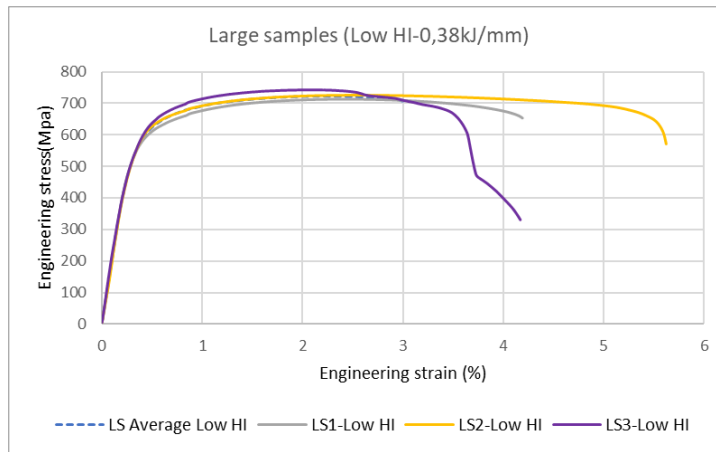


Figure 18. Engineering stress – engineering strain for large size samples (Low HI-LS)

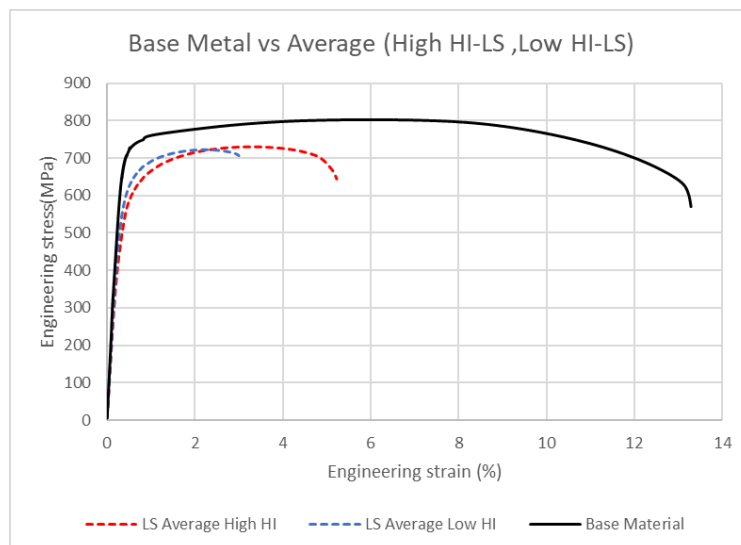


Figure 19. Comparison between average data of weldments (high HI-LS, low HI-LS) and base material (without welding).

The tensile characteristics of all tested samples such as young's modulus  $E$ , yield strength  $f_y$ , strain at yield  $\epsilon_y$ , tensile strength  $f_u$ , and strain at tensile strength  $\epsilon_u$  are presented in table 9 and table 10 for both large and small size samples respectively. Here, the value of yield strength extracted directly from universal testing device, following 0,2% strength value.

Table 9. The mechanical properties of large size weldments compared with Base material.

Sample name	Heat Inputs kJ/mm	$E$ (GPa)	$f_y$ (MPa)	$\epsilon_y$ (%)	$f_u$ (MPa)	$\epsilon_u$ (%)	$(f_u/f_y)$	$(\epsilon_u/\epsilon_y)$
BM		237,99	723,03	0,50	802,65	6,04	1,11	12,08
LS1-Low HI	0,38	203,24	611,24	0,50	712,93	2,42	1,17	4,84
LS2-Low HI		219,58	626,16	0,49	725,51	2,54	1,16	5,18
LS3-Low HI		217,84	634,26	0,49	742,33	2,10	1,17	4,29
	Avg.	213,55	623,89	0,49	726,92	2,35	1,17	4,77
LS1-High HI	0,68	215,22	591,60	0,47	734,84	3,46	1,24	7,36
LS2- High HI		181,93	548,09	0,49	727,93	3,33	1,33	6,79
LS3- High HI		203,53	601,52	0,49	735,33	2,94	1,22	6
	Avg.	200,23	580,40	0,48	732,7	3,24	1,26	6,72

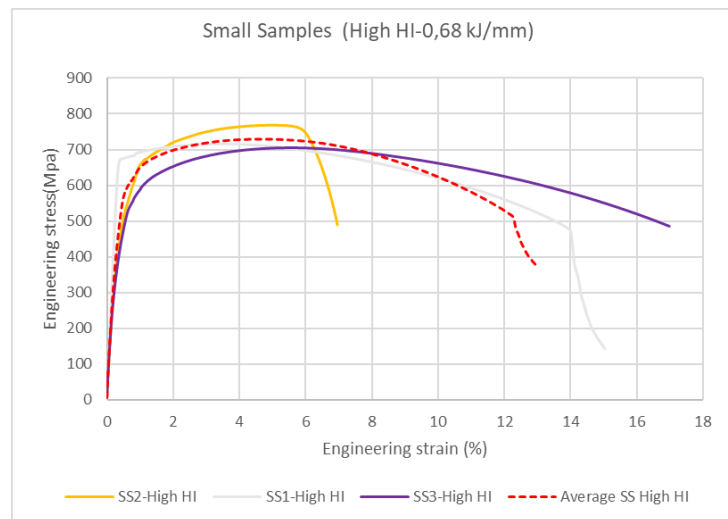


Figure 20. Engineering stress – engineering strain for small size samples (High HI-SS)

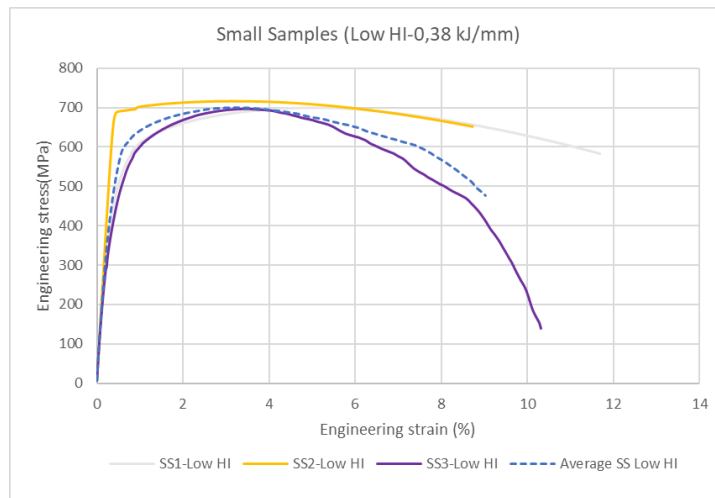


Figure 21. Engineering stress – engineering strain for small size samples (Low HI-SS)

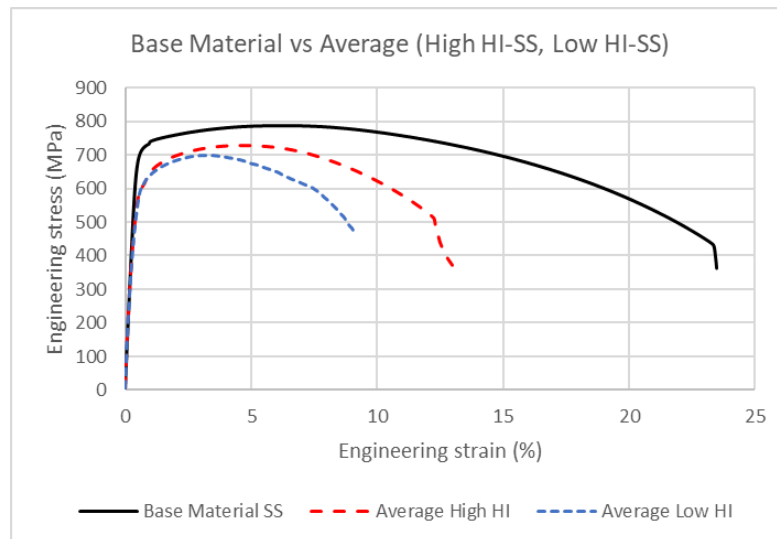


Figure 22. Comparison between average data of small size weldments (high HI-SS, low HI-SS) and base material (without welding).

Table 10: The mechanical properties of small size weldments compared with Base material

Sample name	Heat Inputs kJ/m m	E (GPa)	$f_y$ (MPa)	$\epsilon_y$ (%)	$f_u$ (MPa)	$\epsilon_u$ (%)	$(f_u/f_y)$	$(\epsilon_u/\epsilon_y)$
BM		165.21	708.46	0.62	786.55	6.24	1.11	10.06
SS1-Low HI	0.38	178.99	404.39	0.42	699.57	5.01	1.73	11.92
SS2-Low HI		159.91	593.31	0.57	716.18	3.13	1.23	5.49
SS3-Low HI		142.66	384.69	0.46	696.76	3.47	1.81	7.54
	Avg.	160.52	460.79	0.48	704.17	3.87	1.59	8.32
SS1-High HI	0.68	174.23	557.80	0.52	715.92	3.42	1.28	6.58

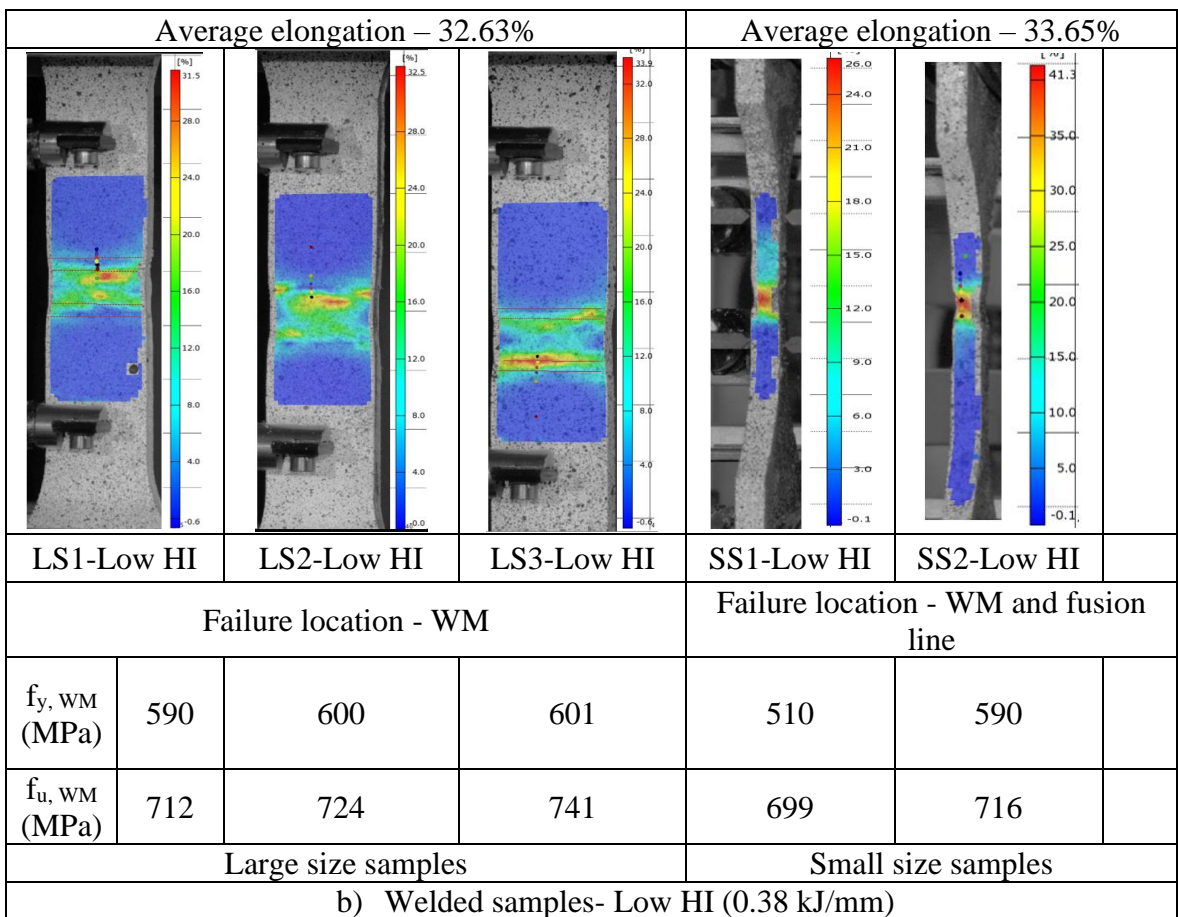
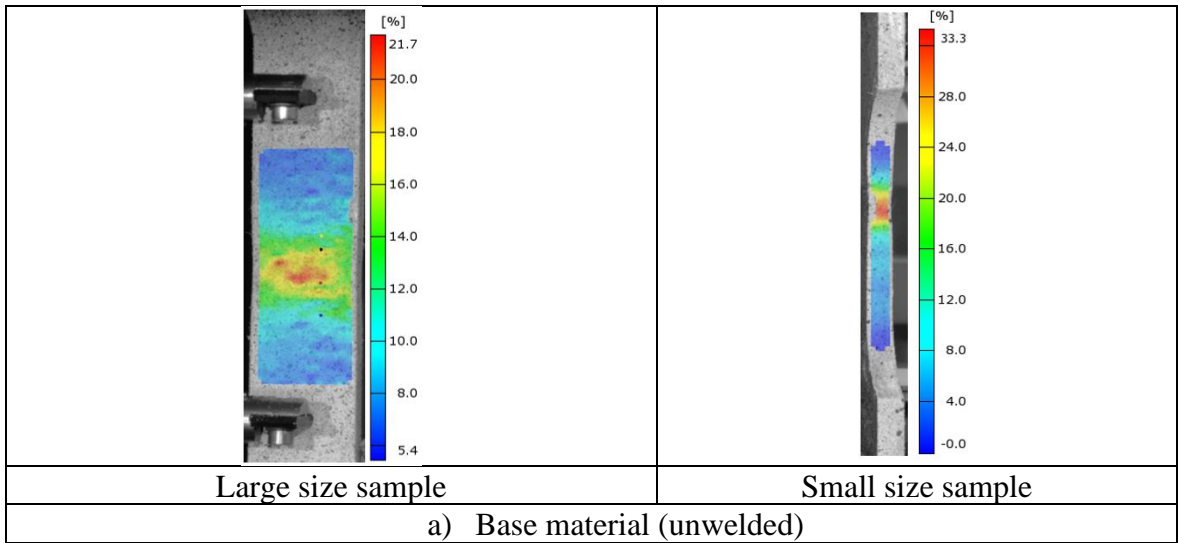
SS2- High HI		145.17	390.39	0.46	768.27	4.94	1.97	10.74
SS3- High HI		167.91	374.22	0.42	705.14	5.57	1.88	13.26
	Avg.	162.43	440.80	0.47	729.78	4.64	1.66	10.19

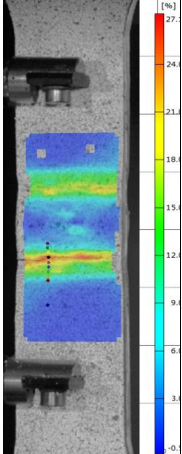
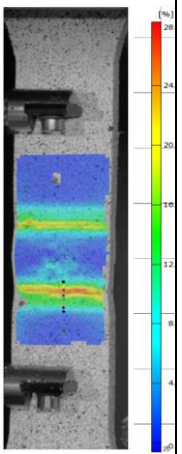
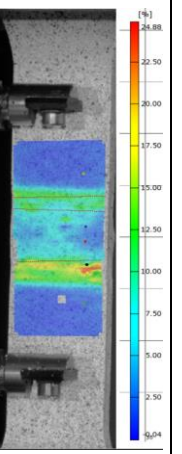
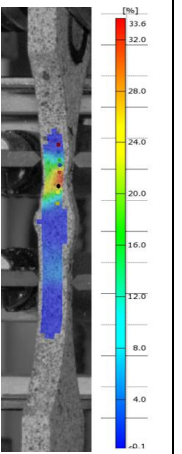
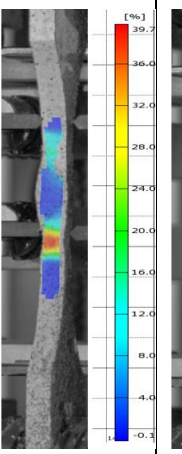
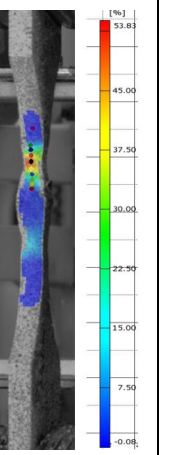
It can be observed from table 9 and table 10, both size tensile properties show almost same mechanical properties, though the yield strength of small size samples shows less strength than large size samples. The gauge length size and the changes of cross section area due to water cut, might be the reason for this yield strength reduction of small size weldments. Moreover, at low heat input, the softening of the weldments happens at weld metal zone and for high input, softening happens at heat affected zones, shown in appendix 1. All tensile tested samples indicate that the strength of welded joints is less than that of base material (BM). For high HI (0,68kJ/mm), the failure happens at HAZ. On the other hand, for low HI (0,38 kJ/mm), the failure happens at WM zone.

4.2 Measurement of local tensile properties of weldments by using 3D optical measurement  
In this study, a 3D optical measurement device (ARAMIS 6.1) was used to evaluate material parameters and observe the local behavior of the weldments, especially at the HAZ, during the tensile test.

Table 11 represents the local behavior for all welded samples including base material samples immediately before failure. These stages were analyzed to track the local mechanical properties of weldments and maximum elongation before fracture of the samples by using digital image correlation techniques. Table 11 shows the local maximum elongations of each case. The elongation at break is showing 21.7% and 33.3% for large and small size base material samples respectively. On the other hand, at low HI energy, the average elongation is 32,63% and 33,65% for large and small size samples respectively. Similarly, at high HI, the average elongation is 26,46% and 42,37% for large and small size samples respectively. The elongation of the weldments of large samples is between 26-32% which is 1.2-1.5 times higher than the elongation of base material, and this is because of softening in the weld zone. Similarly, for small size samples elongation is between 33-42% which is 1-1.2 times higher than that of base material samples. The strength and elongation of the weldments depend on the methods of production of HHSs such as quenching and tempering (QT), direct quenching, thermomechanical rolling with acceleration cooling (TMCP), etc. (Loureiro, 2021, pp. 34-39).

Table 11. Mechanical properties of the failure zone and local deformation prior to failure.



	Average elongation – 26.46%			Average elongation – 42.37%		
						
	LS1-High HI	LS2-High HI	LS3-High HI	SS1-High HI	SS2-High HI	SS3-High HI
	Failure location - HAZ			Failure location - HAZ		
$f_{y, HAZ}$ (MPa)	562	568	563	542	538	543
$f_{u, HAZ}$ (MPa)	734	725	733	715	768	705
	Large size sample			Small size samples		
	c) Welded samples- High HI (0.68 kJ/mm)					

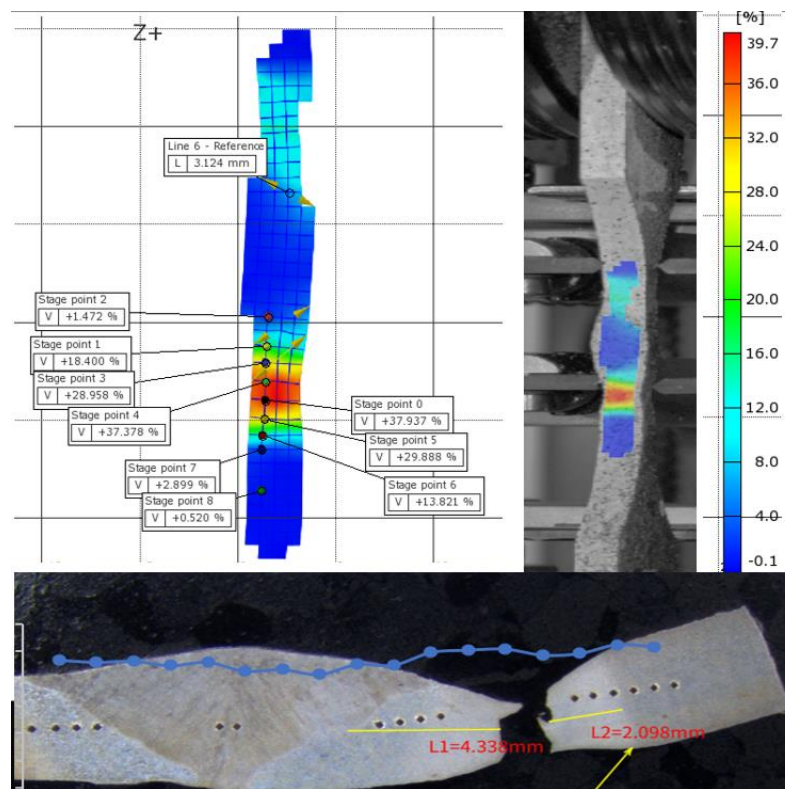
When comparing weldments with base material mechanical properties, the strength reduction of the base plate due to welding is significant. Table 12 shows that for large size samples, the reduced ultimate strength is similar for both low HI and high HI which is 0.91. For small size samples, the reduced ultimate strength for low HI and high HI are 0.89 and 0.93 that of the base material sample (unwelded) respectively. Therefore, due to welding large size and small size weldments show 9 percentage and 7-11 percentage of reduction in ultimate strength respectively.

Table 12. Reduction factors for mechanical properties of welded samples.

Reduction factors, $\alpha$		
	High HI	Low HI
	Ultimate strength ratio, $f_{u, HAZ} / f_{u, BM}$	Ultimate strength ratio, $f_{u, WM} / f_{u, BM}$
Large size	0.91	0.91
Small size	0.93	0.89

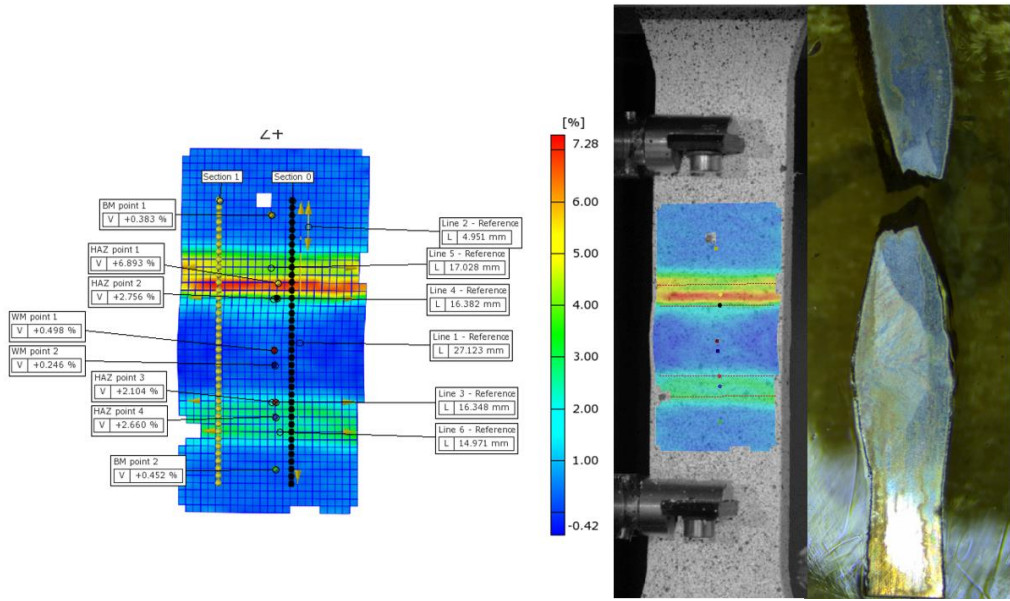
Note: Here  $f_{u, BM}$ , represents tested base material (unwelded) properties.

Deformed samples after polishing and chemical etching and the failure location from ARAMIS are shown in figure 23. Samples after chemical etching can show the exact location of failure. It can be observed from figure 23 that fracture occurs within the weld metal and fusion line for low HI in both large and small size samples. On the other hand, for high HI large samples rupture occurred at the HAZ. Therefore, all deformed samples indicate that the strength of welded joints is less than that of base material (BM). Figure 23 shows the selected point's location and percentage of elongation in three different zones (HAZ, BM, and WM) of the high HI large sample.

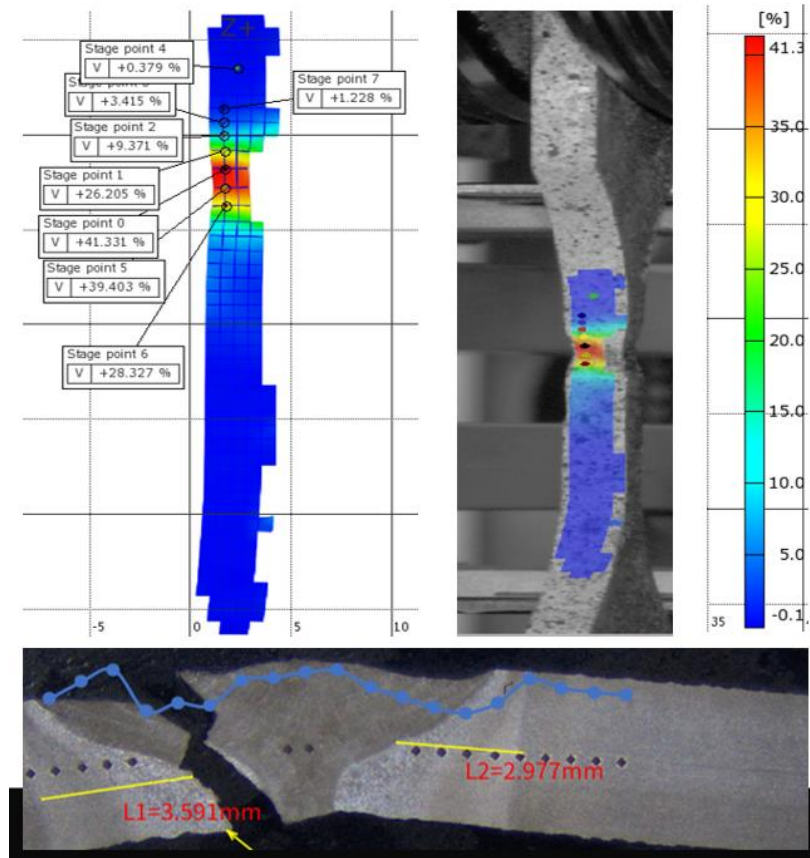


a) SS2-High HI (failure occurs within HAZ)

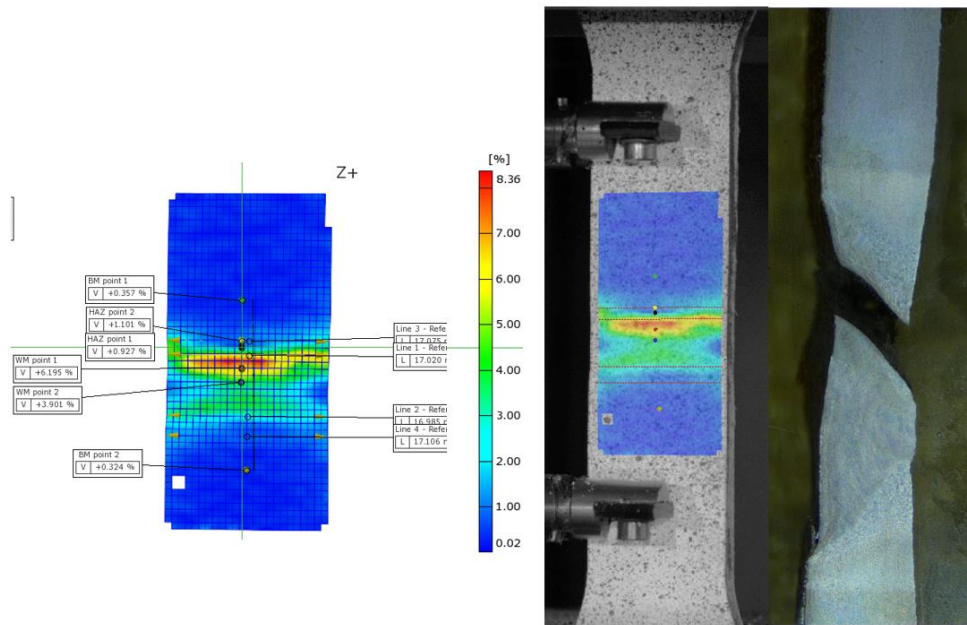




b) LS2-High HI (failure occurs within HAZ)



c) SS2-Low HI (failure occurs within WM and fusion line)



d) LS2-Low HI (fracture occurs within WM and fusion line)

Figure 23. Samples after chemical etching and observed fracture location.

### 4.3 True stress - true strain curve

The stress-strain diagrams of base material obtained by both extensometer and ARAMIS technique are shown in Figure 24. Unlike welded samples, the tensile properties of both small and large size base material samples represent almost similar behavior.

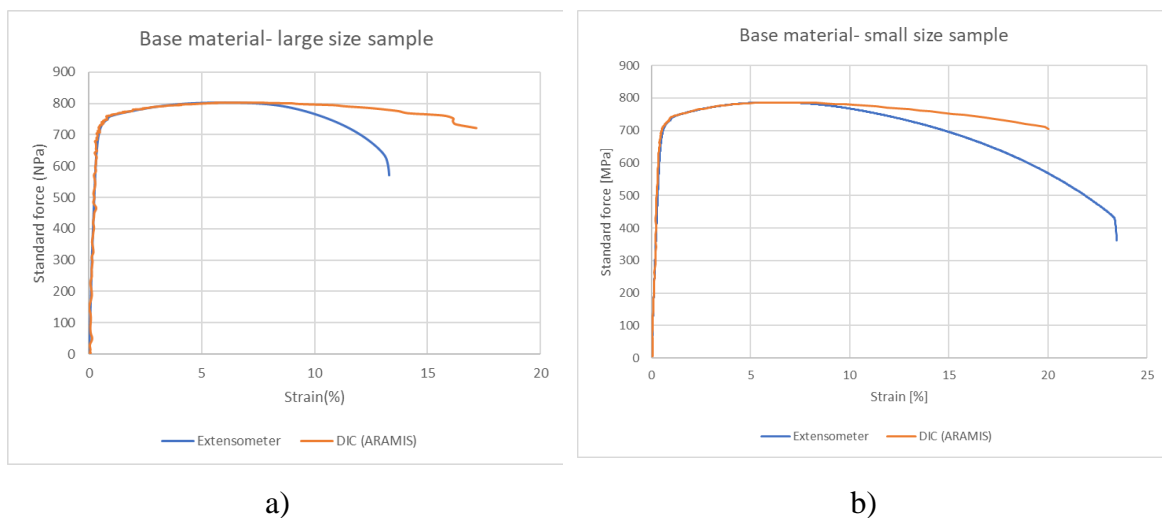


Figure 24: Base material stress-strain diagram obtained by both standard tensile test and DIC technique (ARAMIS) a) Large size sample b) Small size sample.

Due to material heterogeneity, it is challenging to get accurate material properties of the HAZ. DIC (ARAMIS) technique can observe the local strain of the selected zone. As mentioned earlier, the obtained data from ARAMIS software can be used as material input data of LS-Dyna. In this paper, engineering remote stress - true strain data for different zones (BM, WM, and HAZ) of the weldments were obtained from ARAMIS software and universal testing machine (UTM). To get the strain data from ARAMIS measurement, points were taken as a reference from three different local zones (BM, WM, and HAZ) by hardness test profile and visual inspection as shown in Appendix 1. Then, true strain values in each zone at different load stages were calculated by averaging major stains of points data within the same zone. The engineering remote stress ( $\sigma$ ) obtained from the standard tensile testing device was converted to the true stress ( $\sigma_T$ ) by using the following equation,  $\sigma_T = \sigma \times e^{\varepsilon_T}$  where  $\varepsilon_T$  is the true strain. (Younise, 2014); (dynasupport.com, 2021). One example of calculated true input values for high HI (LS-1) data is shown in table 13.

*Table 13: True input values for three different zones of weldments (LS-1, High HI)*

Engineering stress	HAZ true stress	HAZ true strain	BM true stress	BM true strain	WM true stress	WM true strain
(MPa)	(MPa)	(%)	(MPa)	(%)	(MPa)	(%)
593.42	602.26	1.48	595.96	0.43	594.08	0.11
606.47	616.84	1.69	609.09	0.43	607.15	0.11
617.85	631.46	2.18	620.86	0.48	618.64	0.13
627.74	644.04	2.56	630.43	0.43	628.52	0.12
637.00	656.14	2.96	639.70	0.42	637.96	0.15
645.42	667.36	3.34	648.20	0.43	645.96	0.08
655.61	681.31	3.85	658.62	0.46	656.12	0.08
677.33	716.40	5.61	680.38	0.45	678.16	0.12
704.56	772.31	9.18	708.02	0.49	706.11	0.22
724.96	827.41	13.22	728.74	0.52	727.69	0.38
734.49	878.91	17.95	738.71	0.57	739.37	0.66

Table 14 is showing the input data of effective plastic strain and corresponding stress, calculated by subtracting elastic deformation from plastic deformation (dynasupport.com, 2021).

Table 14: Effective plastic strain (EPS) and effective stress (ES) (LS-1, High HI).

Corresponding stress (MPa)	Effective plastic strain (%)		
	HAZ	BM	WM
597.97	0.0	0.00	0.00
612.59	0.24	0.00	0.00
625.76	0.51	0.05	0.02
637.58	0.79	0.00	0.01
649.04	1.11	-0.01	0.04
659.80	1.44	0.00	-0.03
673.97	2.00	0.03	-0.03
707.91	3.66	0.02	0.01
769.29	8.03	0.06	0.11
795.24	8.49	0.09	0.27
810.56	9.09	0.14	0.55

Based on calculated input data, true stress – true strain curves for all samples of low HI are plotted in figures 25-45.

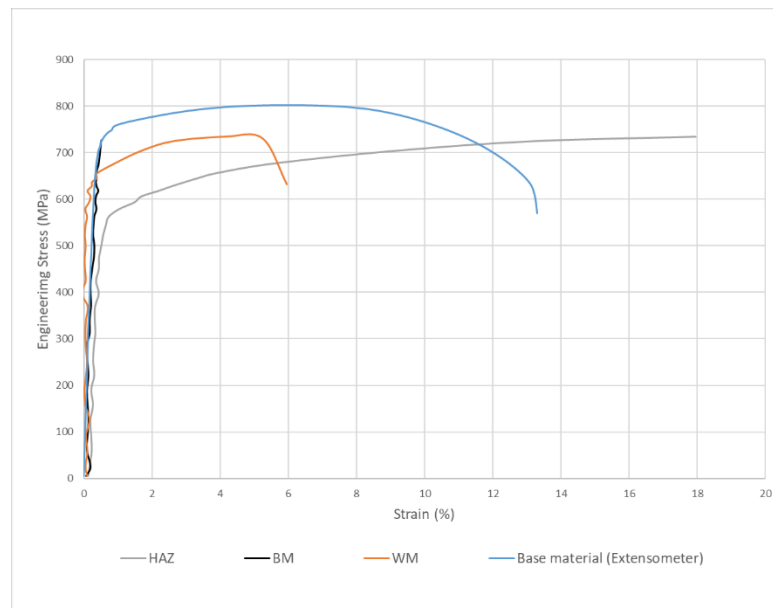


Figure 24. LS1-High HI: Engineering stress – engineering strain (Base material) vs Engineering stress – true strain (BM, WM, and HAZ).

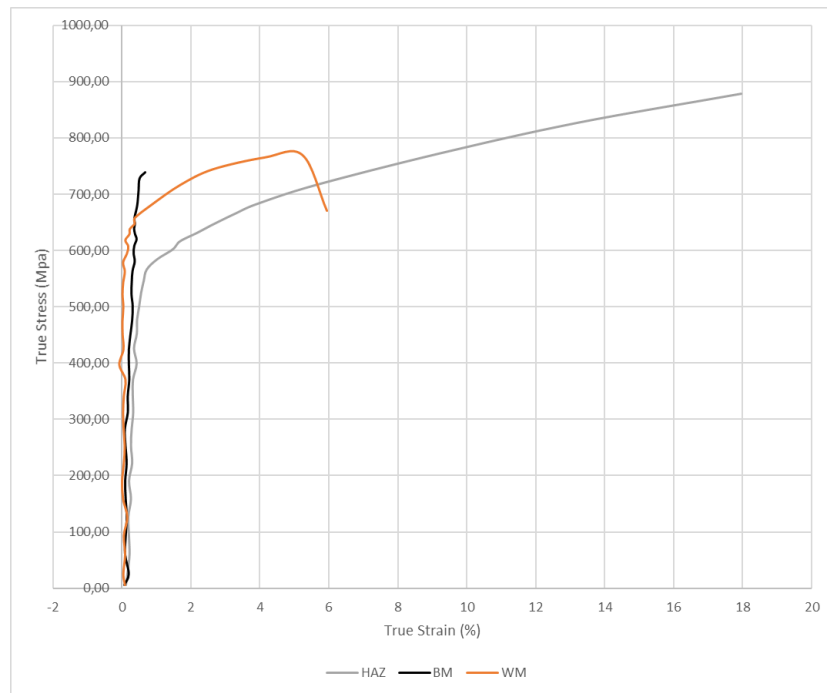


Figure 25. LS1-High HI: True stress – true strain graph (BM,WM, and HAZ)

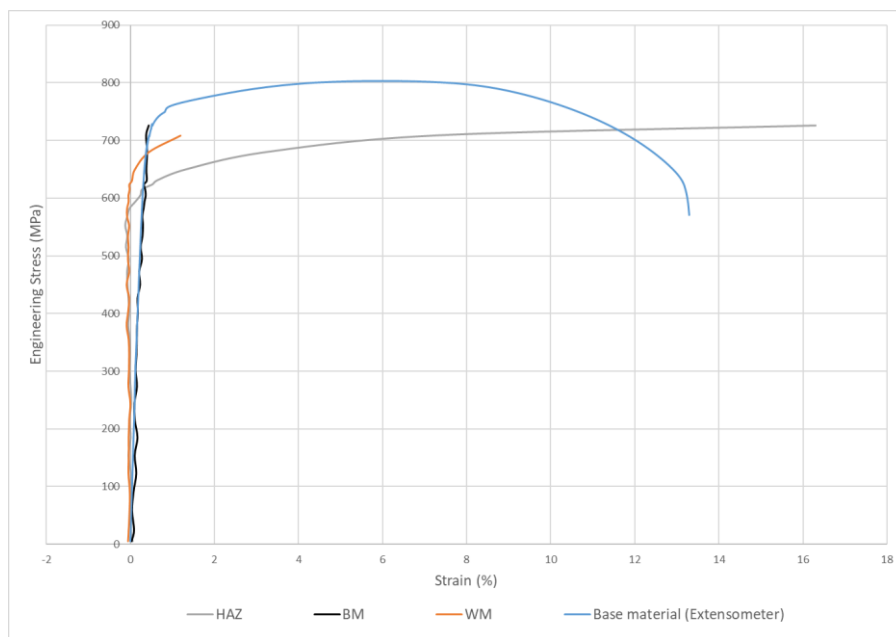


Figure 26. LS2-High HI: Engineering stress – engineering strain (Base material) vs Engineering stress – true strain (BM,WM, and HAZ).

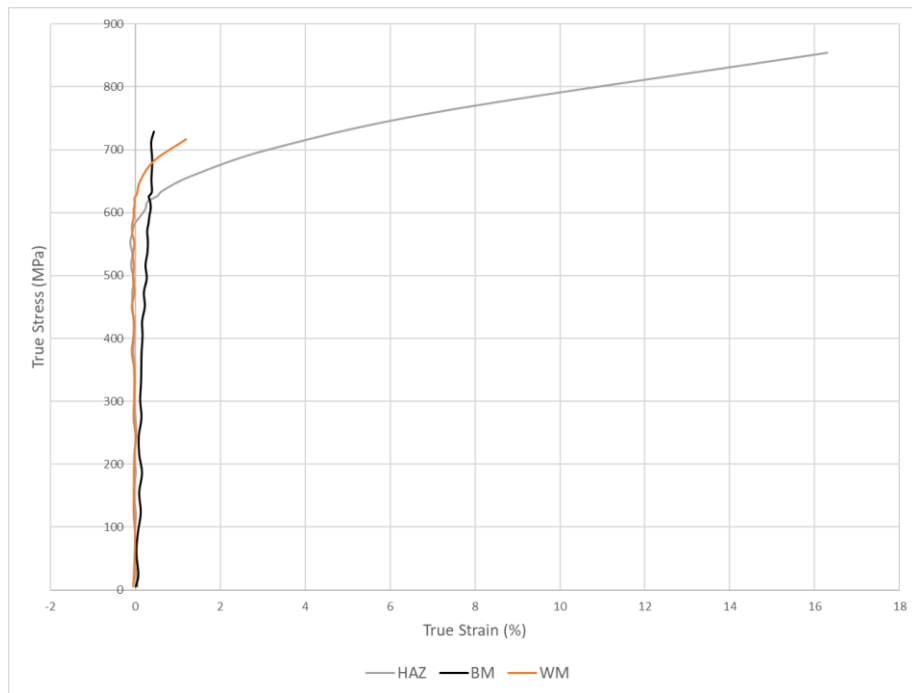


Figure 27. LS2-High HI: True stress – true strain graph (BM,WM, and HAZ)

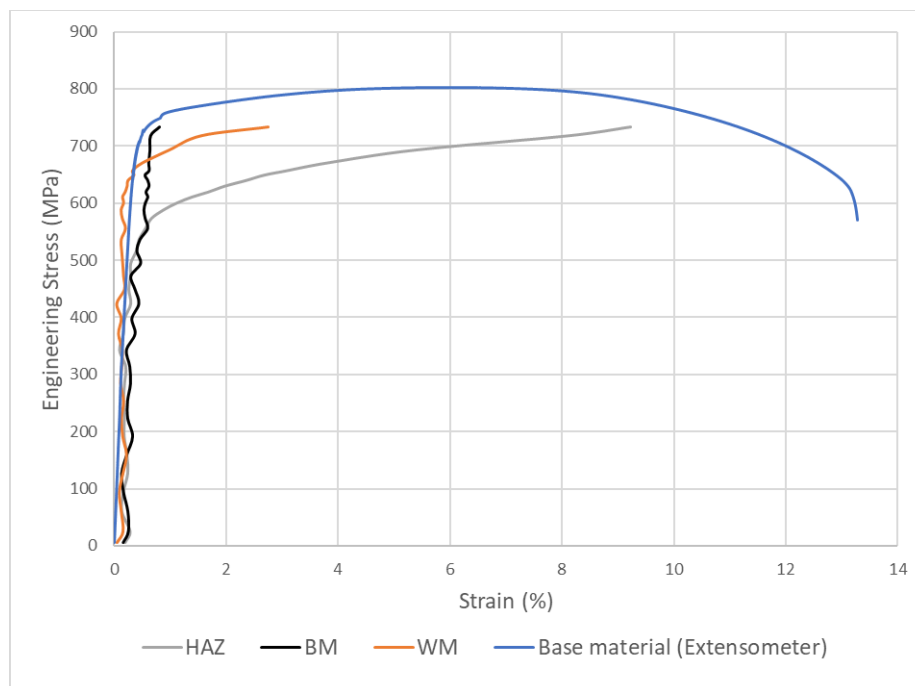


Figure 28. LS3-High HI: Engineering stress – engineering strain (Base material) vs Engineering stress – true strain (BM,WM, and HAZ).

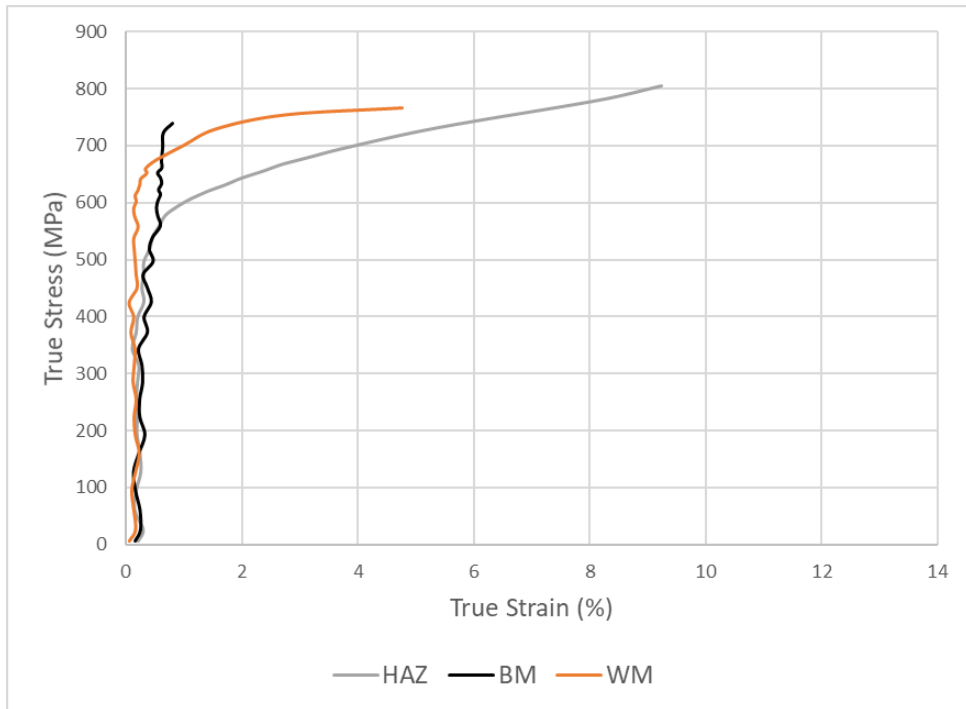


Figure 29. LS3-High HI: True stress – true strain graph (BM,WM, and HAZ)

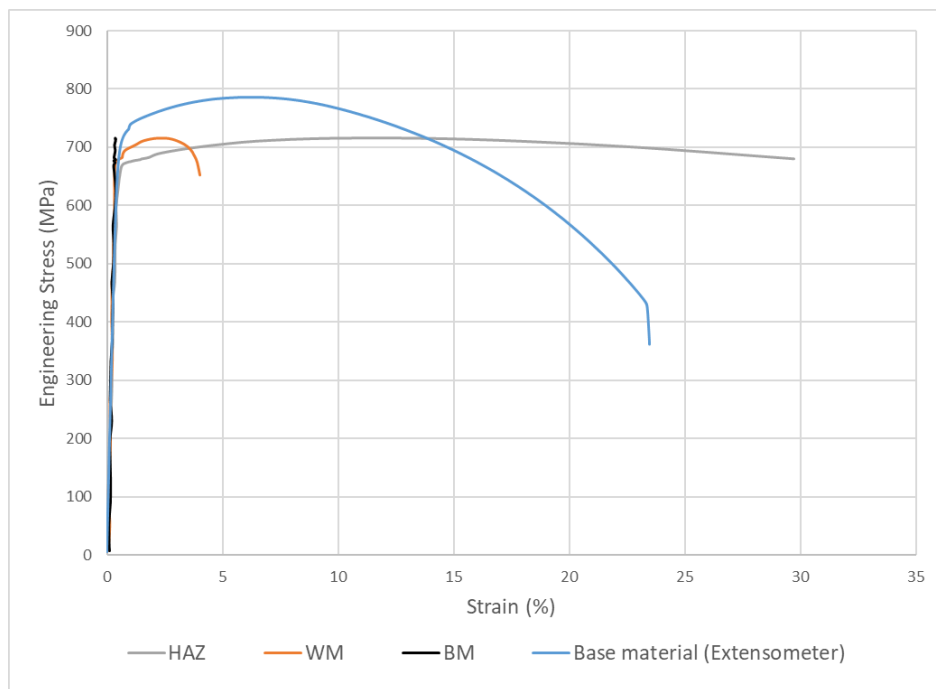


Figure 30. SS1-High HI: Engineering stress – engineering strain (Base material) vs Engineering stress – true strain (BM,WM, and HAZ).

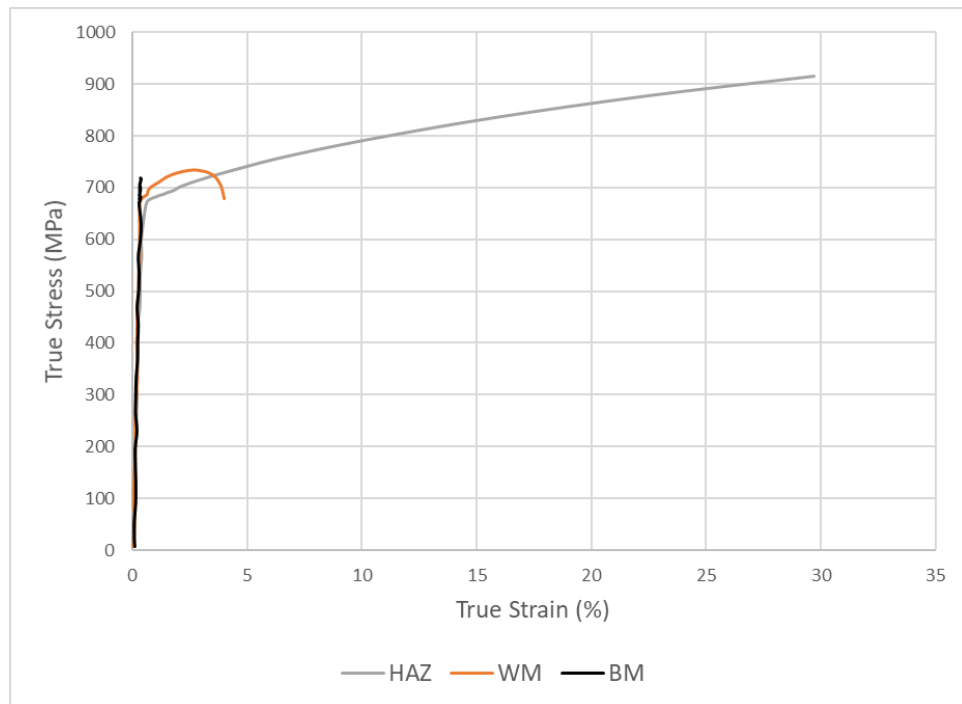


Figure 31. SS1-High HI: True stress – true strain graph (BM,WM, and HAZ)

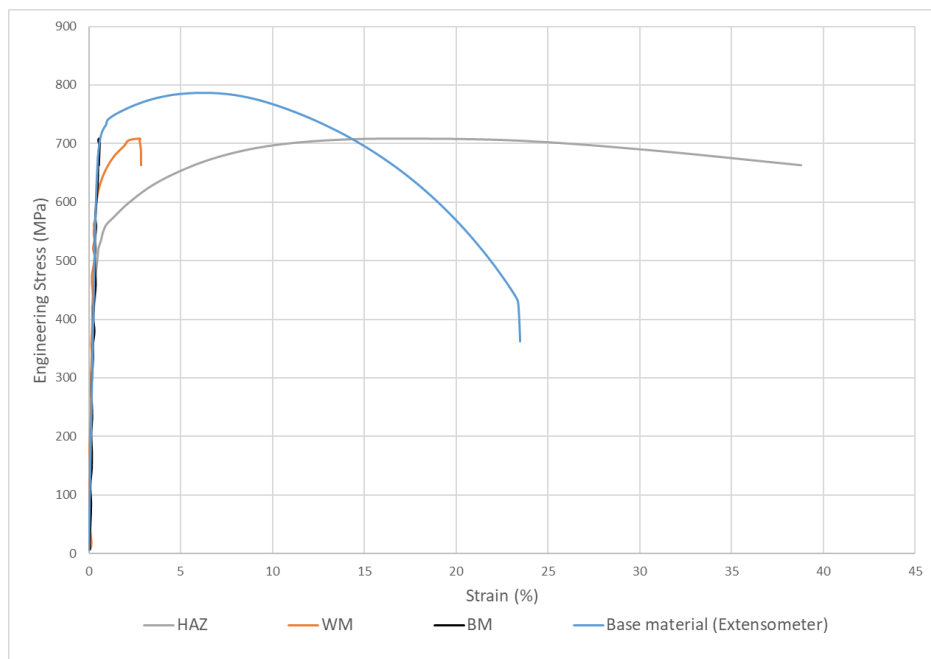


Figure 32. SS2-High HI: Engineering stress – engineering strain (Base material) vs Engineering stress – true strain (BM,WM, and HAZ).



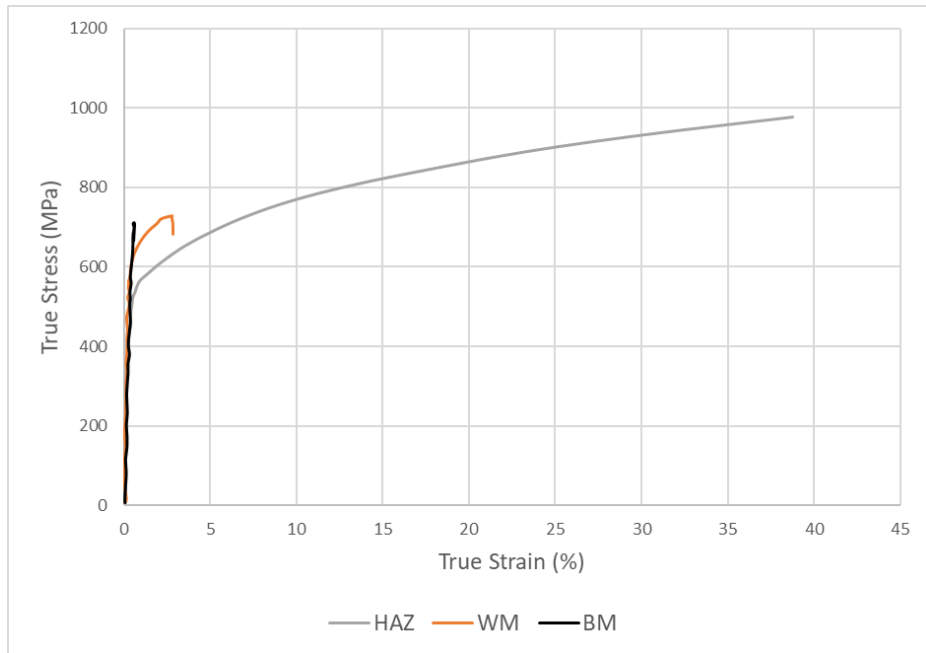


Figure 33. SS2-High HI: True stress – true strain graph (BM,WM, and HAZ)

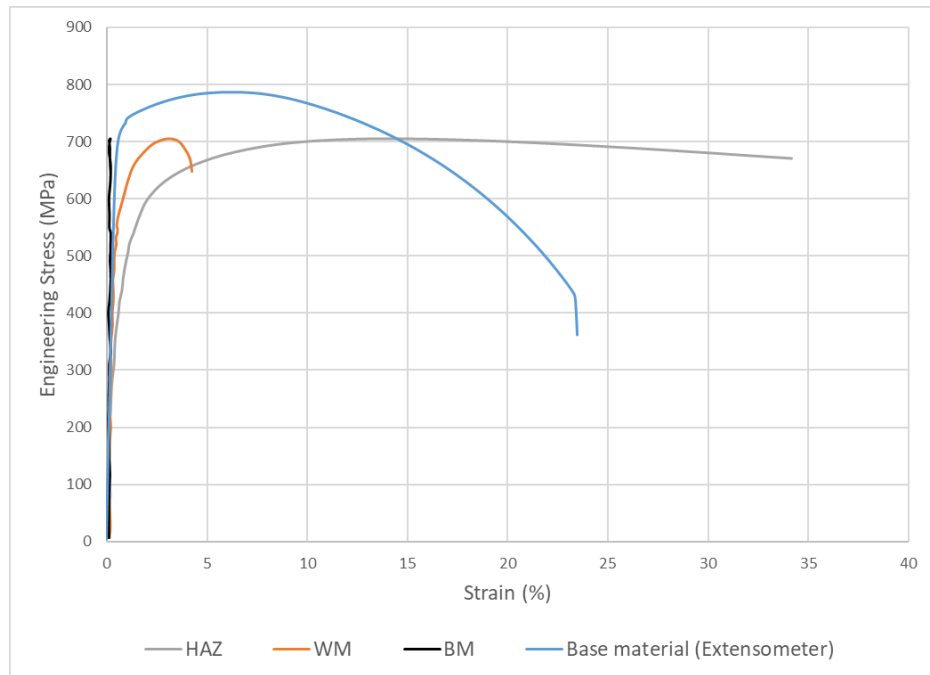


Figure 34. SS3-High HI: Engineering stress – engineering strain (Base material) vs Engineering stress – true strain (BM,WM, and HAZ).

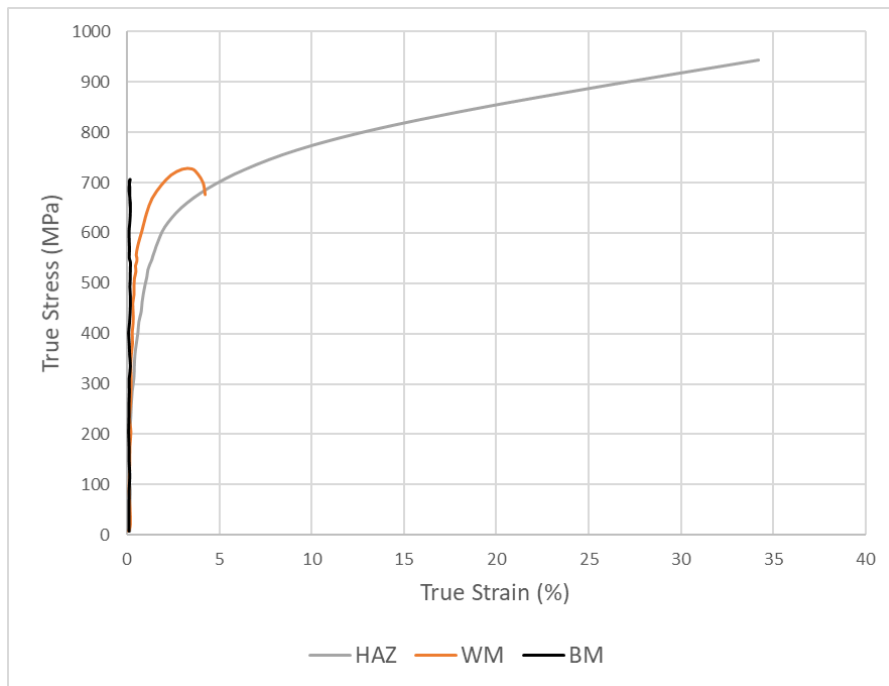


Figure 35. SS3-High HI: True stress – true strain graph (BM,WM, and HAZ)

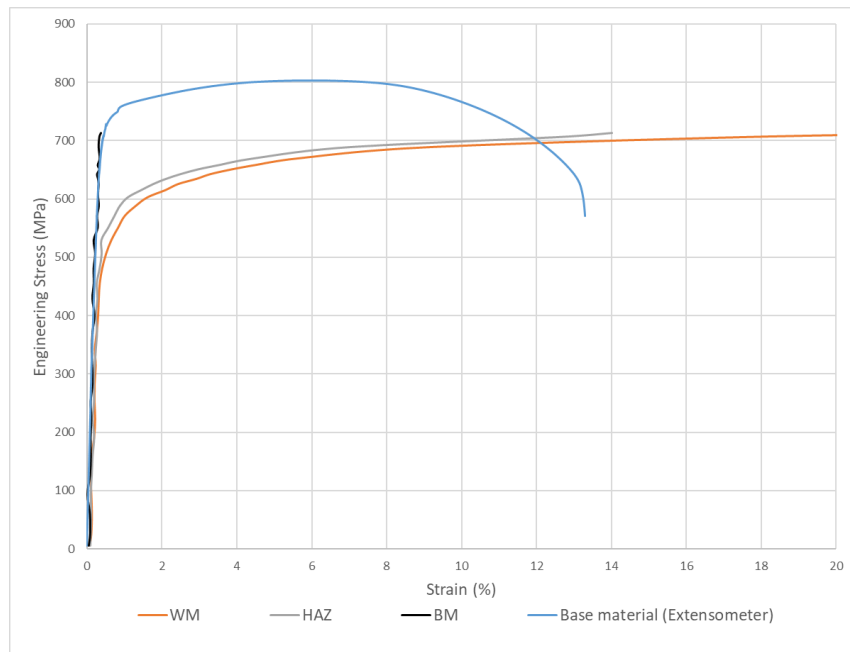


Figure 36. LS1-Low HI: Engineering stress – engineering strain (Base material) vs Engineering stress – true strain (BM,WM, and HAZ).

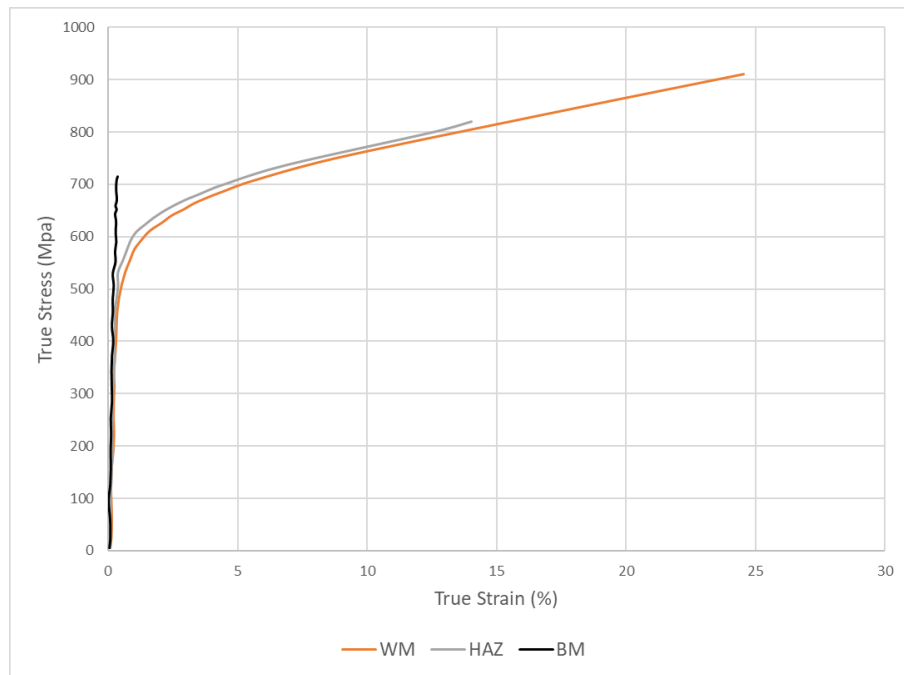


Figure 37. LS1-Low HI: True stress – true strain graph (BM,WM, and HAZ)

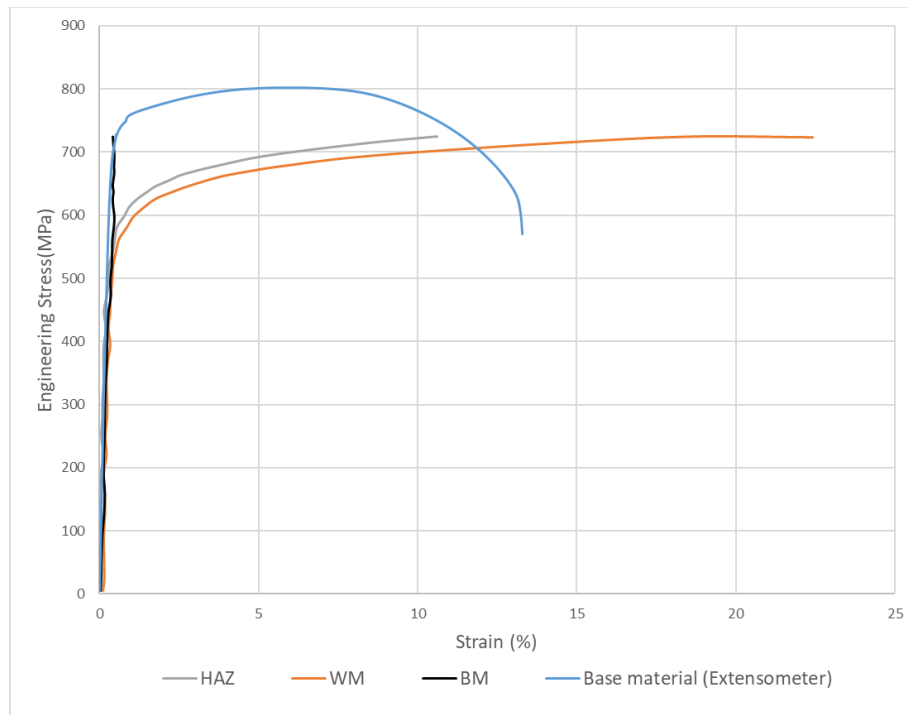


Figure 38. LS2-Low HI: Engineering stress – engineering strain (Base material) vs Engineering stress – true strain (BM,WM, and HAZ).

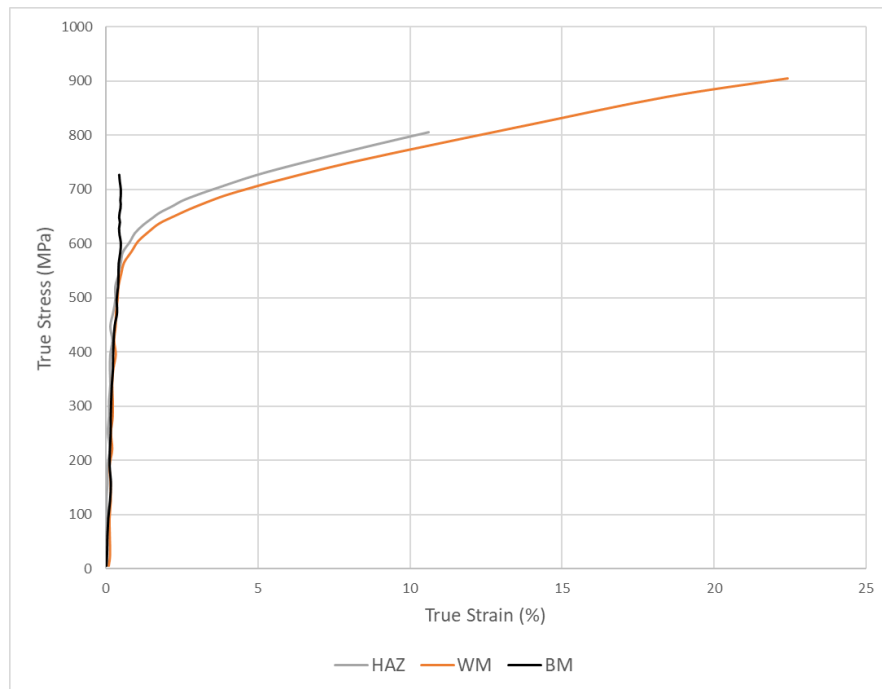


Figure 39. LS2-Low HI: True stress – true strain graph (BM,WM, and HAZ)

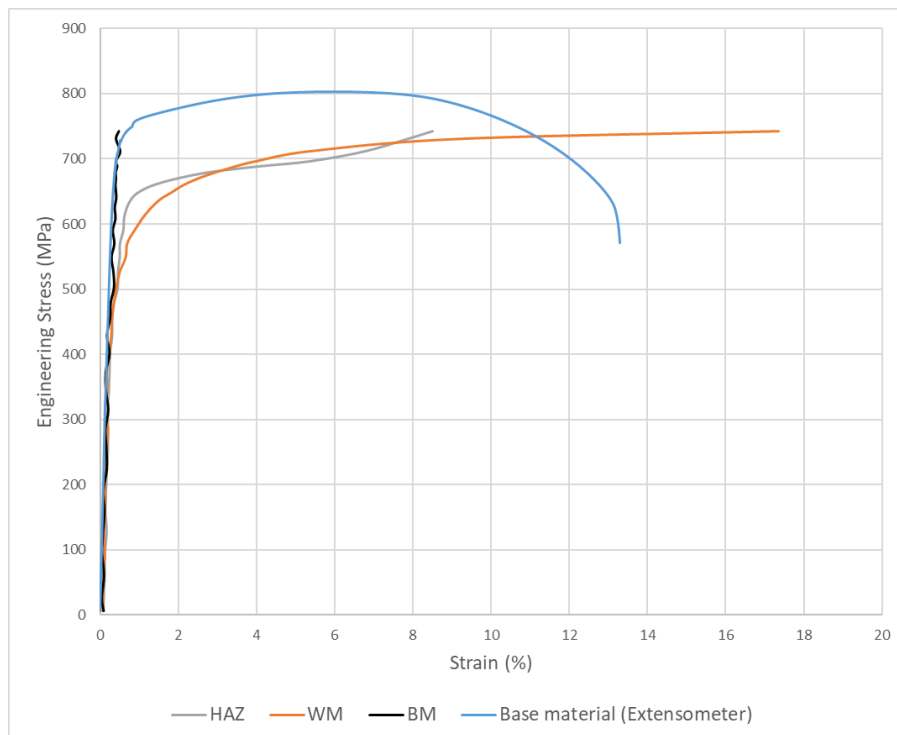


Figure 40. LS3-Low HI: Engineering stress – engineering strain (Base material) vs Engineering stress – true strain (BM,WM, and HAZ).

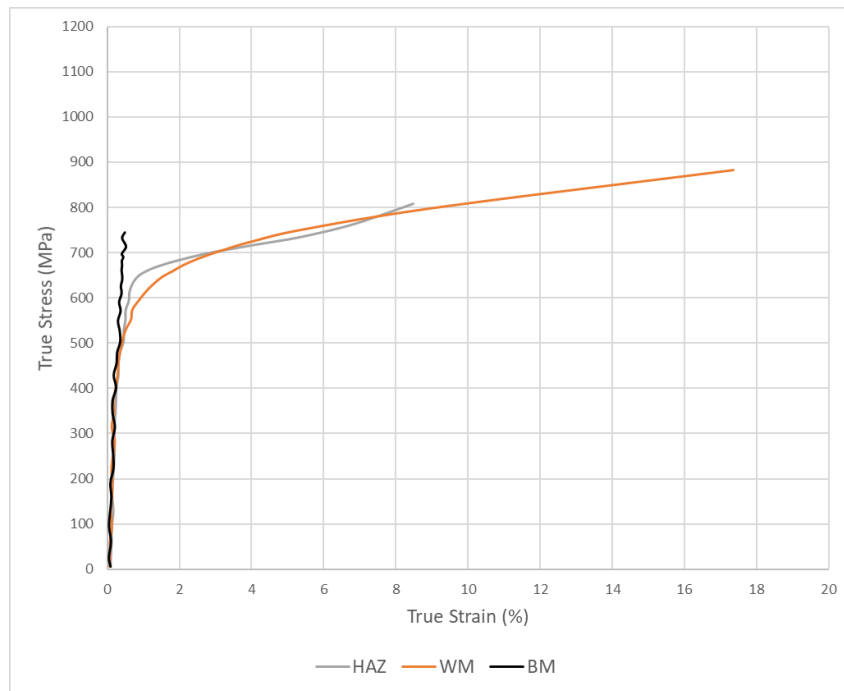


Figure 41. LS3-Low HI: True stress – true strain graph (BM,WM, and HAZ)

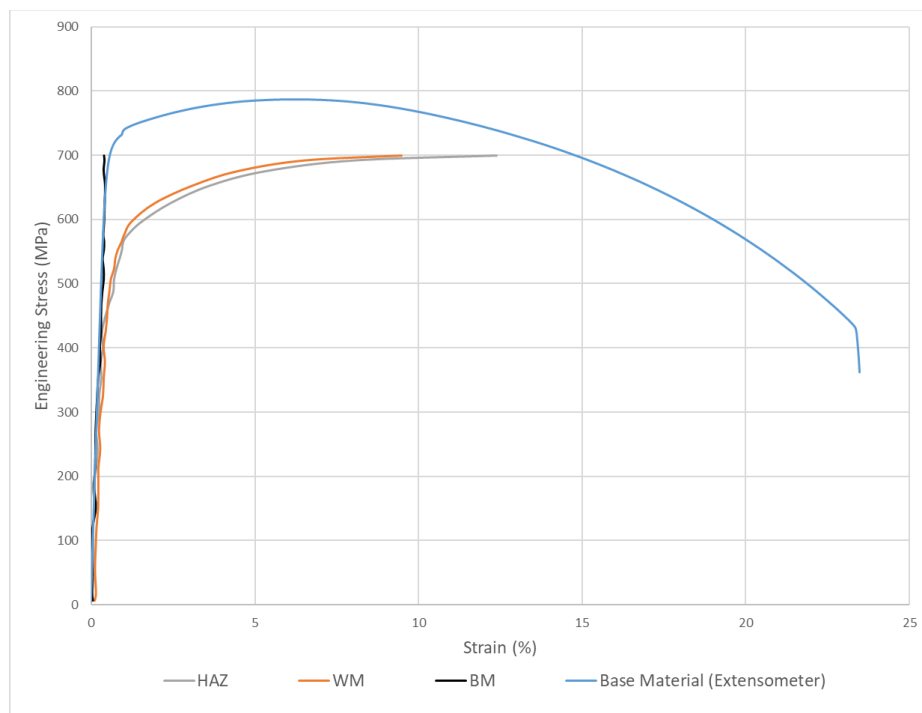


Figure 42. SS1-Low HI: Engineering stress – engineering strain (Base material) vs Engineering stress – true strain (BM,WM, and HAZ).

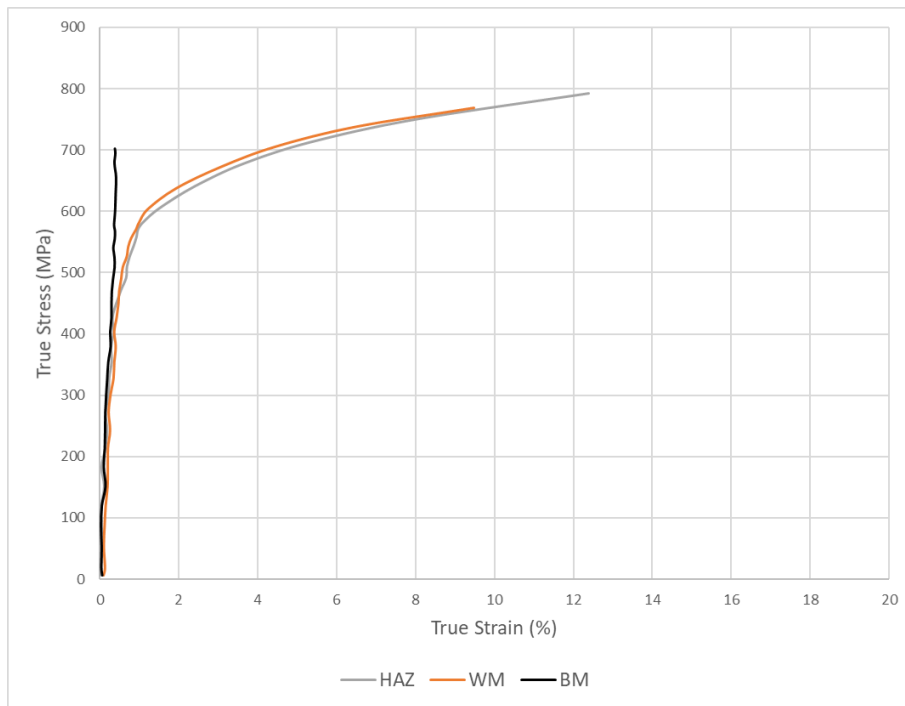


Figure 43. SS1-Low HI: True stress – true strain graph (BM,WM, and HAZ)

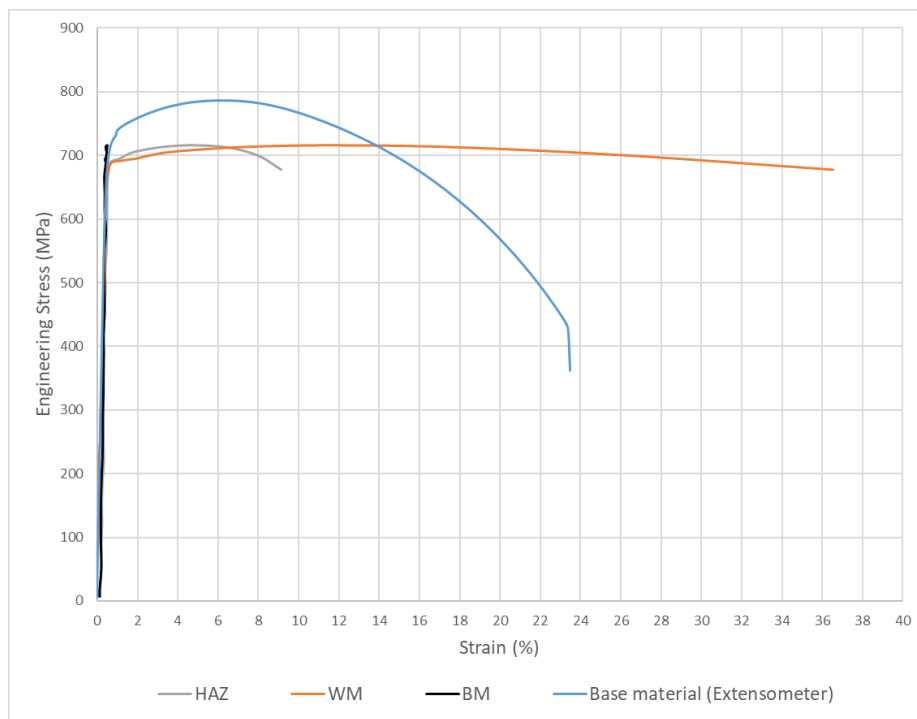


Figure 44. SS2-Low HI: Engineering stress – engineering strain (Base material) vs Engineering stress – true strain (BM, WM, and HAZ).

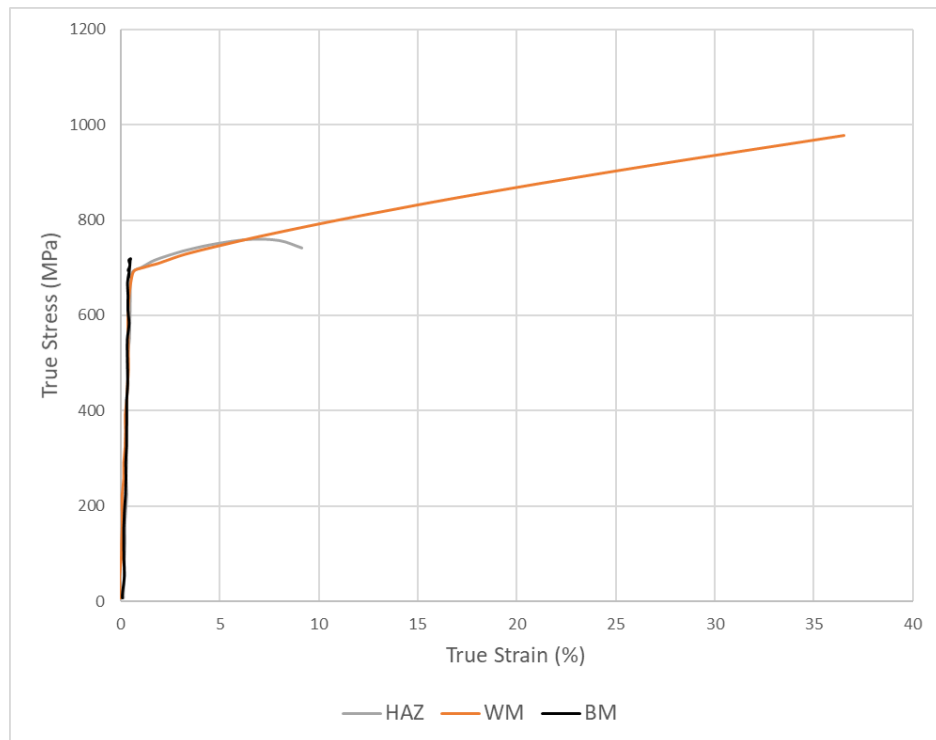


Figure 45. SS2-Low HI: True stress – true strain graph (BM,WM, and HAZ)

#### 4.4 Principle strain direction and rupture path

The load capacity of the high-strength steels weldments can be affected by the softening effect in HAZ, unlike conventional mild or low strength steels weldments (Maurer et al., 2015). Such reduction of the capacity can be avoided by designing weld joints in such a way that it is inclined in the direction of the loading (Björk, Nykänen and Valkonen, 2016, pp. 139-140). Figure 46 shows the potential critical failure planes for axially loaded plate with different angles.

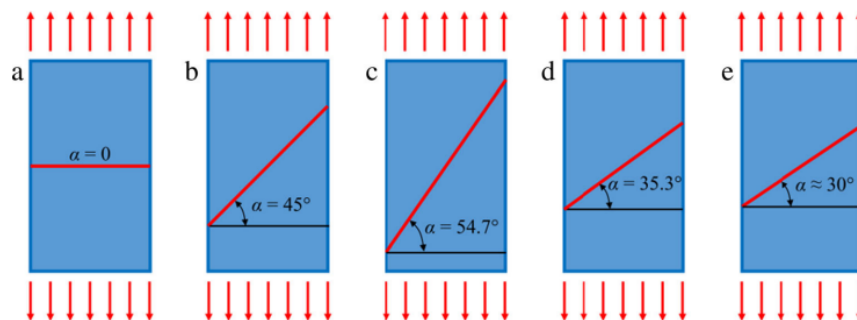


Figure 46. The potential critical failure planes for axially loaded plates with different angles (Björk, Nykänen and Valkonen, 2016, p. 141).

When  $\alpha = 0$ , there is no shear stress, the fracture happens perpendicular to the applied force. This type of material is typically brittle. On the other hand,  $\alpha = 45$  represents maximum shear stress. This angle of 45 degrees has huge consequences for ductile materials which tend to fail in directions in which the shear stress is maximum (Dowling, 2007, pp. 123-129.). It can be observed from figure 47 that for both low and high input in the plate thickness direction, the critical plane shows nearly 45 degrees in single (/) failure plane.

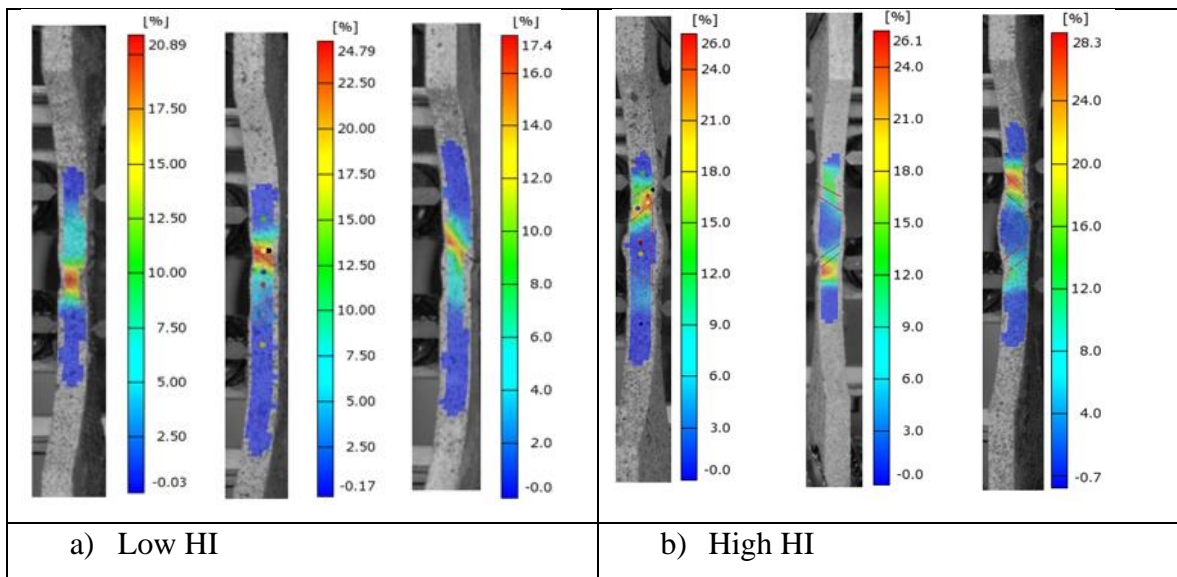


Figure 47. Direction of critical plane

Figure 48 shows ARAMIS data of the major strain direction of the weldments at the stage of ultimate tensile stress. It can be observed that the major strain direction in the critical region shows perpendicular to the local strain coordinate system. Though, the rupture path shows a nearly 45-degree angle. In that case, the failure mood happens in the butt weld with thin plate.



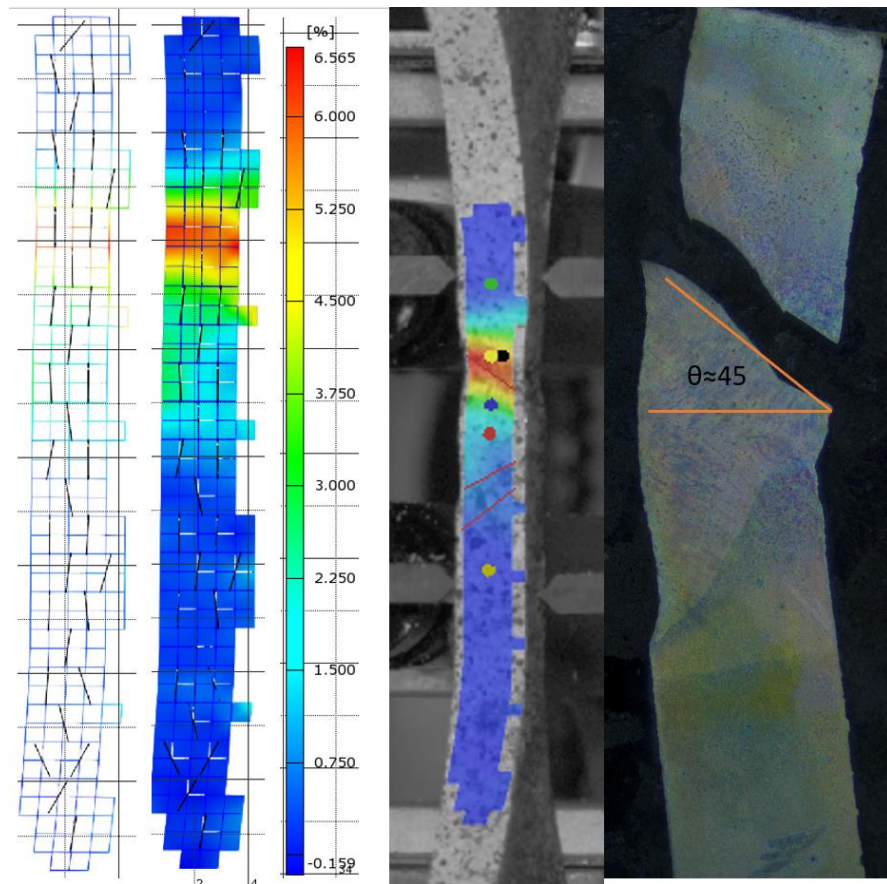


Figure 48: Major strain direction of the weldment at ultimate tensile stress.

It should be noted that ARAMIS 3D optical measurement systems require a stochastic pattern to track and identify reference points. It is difficult to track and identify points from deformed samples after necking, as the stochastic pattern on the surface of the samples is also distorted. Therefore, finite element analysis (FEA) can predict the failure angle more accurately. Björk et al. (2016), utilized LS-DYNA and ABAQUS FEM tools for analyzing failure angle.

## 5 DISCUSSION AND CONCLUSIONS

This research paper aims to find out the stress-strain relationship of S700 weldments of two different heat inputs. Butt-welded V-shaped joints with plate thickness of 4 mm were used. The universal testing machine cannot predict accurately the material behavior of the welded samples due to material heterogeneity in the weld zones (BM, WM, and HAZ). To overcome this challenge, this research applies DIC technique (ARAMIS) for evaluating tensile properties of all different zones of a weldment. True stress- true strain curves of high-strength steel welded joint zones were estimated and plotted by using tensile tests results and 3D optical strain measurement test results.

Three zones of the weldments were marked based on hardness test profile and visual inspection. Two different sets of samples were tested, one set with standard size of tensile test specimens, and the other set with small size corresponding to the size of Gleeble test specimens. Test result data comparison between the universal testing machine with extensometer and ARAMIS test results for both size unwelded samples (base metal samples) show almost similar mechanical properties. Therefore, it can be concluded that the 3D optical strain measurement device (ARAMIS) can predict the strain and displacement properties of the materials precisely.

The true strain- true stress data obtained show yield and ultimate tensile strength of base metal, HAZ and weld zones. ARAMIS test results identify the critical stress zone where failure is initiated. These test results can be used in finite element modelling, for increasing the accuracy when predicting tensile test behavior of welded joints with studied geometry.

All tensile tested samples indicate that the strength of welded joints is less than that of base material (BM). For high HI (0,68kJ/mm), the failure happens at HAZ. On the other hand, for low HI (0,38 kJ/mm), the failure happens at WM zone. The failure in the weld zones may be explained due to adverse development of residual stress and metallurgical changes.

Further tests should be done incorporating different material thicknesses and observe the effects of welding parameters in the joint properties. A better understanding of how to weld

HSSs will encourage a wider use of these steels. The possible development of a universal WPS through laboratory testing of weld joint properties, will increase the possibilities to replace lower grade steels with higher grade steels in different industries and applications.

## 6 SUMMARY

The main objective of this thesis is to determine true stress and true strain curve for three different zones of welded joints. For future research, those experimental results can be utilized to simulate tensile testing welded joint samples with finite element modelling. In this thesis, welded joints made of high strength steel S700 are examined with two different heat inputs. The main research problem of this research is to determine true stress and true strain curve for three different zones of the welded joints and analyze the local behavior of the joints. To solve this research problem, first research question that arises is to find out the way of determining local mechanical properties of welded joints. Digital image correlation (DIC) technique was utilized for observing local behavior during tensile test of the samples. Prior to the test, 3D scan was carried to get actual cross section area. Both tensile tests and 3D optical measurement processes were carried out simultaneously to observe the local behavior of welded joints. By combination of both test results, true stress and true strain curves are plotted. From ARAMIS 3D optical measurement device, true strain data for different zones of the weldment was obtained. True stress data was obtained from tensile testing device by converting engineering stress to true stress. The obtained data can be used as material input data of LS-Dyna for simulating welded joints with actual HAZ properties. Moreover, this thesis compares the teste results of welded samples with base material teste samples to observe the changes of mechanical properties. The experimental results show that the strength of the weldments is lower than that of the base material and fracture was initiated at WM zone for low heat input and at HAZ for high heat input.

## REFERENCES

- Amraei, M., Dabiri, M., Björk, T. and Skriko, T., 2016. Effects of Workshop Fabrication Processes on the Deformation Capacity of S960 Ultra-high Strength Steel. *Journal of Manufacturing Science and Engineering*, 138(12), pp.7-8.
- Azhari, F., Heidarpour, A., Zhao, X. and Hutchinson, C., 2017. Post-fire mechanical response of ultra-high strength (Grade 1200) steel under high temperatures: Linking thermal stability and microstructure. *Thin-Walled Structures*, 119, pp.114-125.
- Arora, A., Roy, G. and DebRoy, T., 2010. Cooling rate in 800 to 500°C range from dimensional analysis. *Science and Technology of Welding and Joining*, 15(5), pp.423-427.
- Berdnikova, O., Sydorets, V. and Alekseenko, T., 2014. Structure and Properties of Laser-Welded Joints from High-Strength Steels. *Applied Mechanics and Materials*, 682, pp.240-245.
- Bowditch, W., 2010. *Welding technology fundamentals*. Tinley Park, Ill.: Goodheart-Willcox Company, pp.54-59.
- Björk, T., Nykänen, T. and Valkonen, I., 2016. On the critical plane of axially loaded plate structures made of ultra-high strength steel. *Welding in the World*, 61(1), pp.139-150.
- Collin, P., Möller, M. and Nilsson, M., 2009. Under matching butt welds in high strength steel. In: *International association for bridge and structural engineering symposium, Bangkok 2009: sustainable infrastructure – environment friendly, Safe and resource efficient*, 11, pp.96-106.
- CEWELD, 2021. ER 100 S-G. [online] [Arcweldingservice.com](https://www.arcweldingservice.com/product/product_detail/1148). Available at: <[https://www.arcweldingservice.com/product/product\\_detail/1148](https://www.arcweldingservice.com/product/product_detail/1148)> [Accessed 15 September 2021].
- Dowling, N., 2007. *Dowling NE (2007) Mechanical behavior of materials: engineering methods for deformation, fracture, and fatigue*,. 3rd ed. New Jersey: Prentice Hall, pp. 123-129.
- EN 1011-2 D4, 2001. *Welding. Recommendations for welding of metallic materials. Part 2: Arc welding of ferritic steels*, s.l.: s.n.
- Esabna.com. 2021. Heat input and its effects on material properties. [online] Available at: <<https://www.esabna.com/us/en/education/blog/heat-input-and-its-effects-on-material-properties.cfm>> [Accessed 7 September 2021].
- Farrokhi, F., Siltanen, J. and Salminen, A., 2015. Fiber Laser Welding of Direct-Quenched Ultrahigh Strength Steels: Evaluation of Hardness, Tensile Strength, and Toughness Properties at Subzero Temperatures. *Journal of Manufacturing Science and Engineering*, 137(6), pp. 9-15.

- Guo, W., Crowther, D., Francis, J., Thompson, A., Liu, Z. and Li, L., 2015. Microstructure and mechanical properties of laser welded S960 high strength steel. *Materials & Design*, 85, pp.534-548.
- Guo, W., Li, L., Dong, S., Crowther, D. and Thompson, A., 2017. Comparison of microstructure and mechanical properties of ultra-narrow gap laser and gas-metal-arc welded S960 high strength steel. *Optics and Lasers in Engineering*, 91, pp.1-15.
- Gleeble.com. 2021. Gleeble 3800-GTC. [online] Available at: <<https://www.leeble.com/products/leeble-systems/leeble-3800.html>> [Accessed 9 September 2021].
- Gourd, L., 1995. Principles of welding technology. London: E. Arnold, pp.45-49.
- Greicevci, B., 2020. Macroscopic photo taken from the research laboratory in Häme University of Applied Sciences. Hämeenlinna, Finland: s.n, p. 23.
- Hajro, I., Hodzic, D. and Tasic, P., 2017. Mechanical Properties of Heat-Affected Zone of High-Strength Steel Welds. p.0611.
- Havula, J., Garifullin, M., Heinisuo, M., Mela, K. and Pajunen, S., 2018. Moment-rotation behavior of welded tubular high strength steel T joint. *Engineering Structures*, 172, pp.523-537.
- Jovicic, R., 2017. Possibilities of predicting the behaviour of ferrite-austenite welded joints in pressure equipment during exploitation. *Tehnicki vjesnik - Technical Gazette*, 24(5), pp. 28-42.
- Ling, Y., 1996. Y. Ling, Uniaxial True Stress-Strain after Necking, 5 (1996) 37–48. *AMP Journal of Technology*, 5, pp.37-48.
- Kim, Y. and Schwalbe, K., 2001. Heat affected zone cracks. Geesthacht: GKSS-Forschungszentrum, pp. 4-9.
- Khurshid, M., Barsoum, Z. and Mumtaz, N., 2012. Ultimate strength and failure modes for fillet welds in high strength steels. *Materials & Design*, 40, pp.36-42.
- Lee, J., Park, S., Kwon, H., Kim, G. and Lee, C., 2014. Laser, tungsten inert gas, and metal active gas welding of DP780 steel: Comparison of hardness, tensile properties and fatigue resistance. *Materials & Design*, 64, pp.559-565.
- Loureiro, A., 2021. Effect of heat input on plastic deformation of undermatched welds, pp.34-39.
- LS-DYNA, 2021. From engineering to true strain, true stress. [online] Welcome to the LS-DYNA support site. Available at: <<https://www.dynasupport.com/howtos/material/from-engineering-to-true-strain-true-stress>> [Accessed 1 November 2021].
- Mitrovic, N., 2011. Application and Mode of Operation of Non-Contact Stereometric Measuring System of Biomaterials. *FME Transactions*, 39, pp 24-29.

- Milosevic, M. and Mitrovic, N., 2011. Digital image correlation analysis of biomaterials. IEEE International Conference on Intelligent Engineering Systems, pp. 25-29.
- Milošević, N., Sedmak, A., Bakić, G., Lazić, V., Milošević, M., Mladenović, G. and Maslarević, A., 2021. Determination of the Actual Stress–Strain Diagram for Undermatching Welded Joint Using DIC and FEM. *Materials*, 14(16), p.4691.
- Milosevic, N., Younise, B., Sedmak, A., Travica, M. and Mitrovic, A., 2021. Evaluation of true stress–strain diagrams for welded joints by application of Digital Image Correlation. *Engineering Failure Analysis*, 128, p.105609. Milosevic, M., 2021. Measurement of local tensile properties of welded joint using Digital Image Correlation method. p.485.
- Milosevic, M., Milosevic, N. and Sedmak, S., 2016. Digital image correlation in analysis of stiffness in local zones of welded joints. *Tehnicki vjesnik - Technical Gazette*, 23(1), pp. 23-27.
- Milošević, N., Sedmak, A., Bakić, G., Lazić, V., Milošević, M., Mladenović, G. and Maslarević, A., 2021. Determination of the Actual Stress–Strain Diagram for Undermatching Welded Joint Using DIC and FEM. *Materials*, 14(16), p.4691.
- Maurer, W., Ernst, W., Rauch, R., Vallant, R. and Enzinger, N., 2015. Evaluation of the factors influencing the strength of HSLA steel weld joint with softened HAZ. *Welding in the World*, 59(6), pp.809-822.
- Ngo, D., 2021. Finite element simulation of heat affected zone of welded joint in high strength steel.. Hämeenlinna University Centre, *Construction Engineering*, pp. 12-15.
- Nejković, M., 2019. New method for determining cooling time and preheating temperature in arc welding. *Thermal Science*, 23(6 Part B), pp. 3975-3984.
- Milosevic, N., Younise, B., Sedmak, A., Travica, M. and Mitrovic, A., 2021. Evaluation of true stress–strain diagrams for welded joints by application of Digital Image Correlation. *Engineering Failure Analysis*, 128, p.105609.
- Muthusamy, C., Karuppiyah, L., Paulraj, S., Kandasami, D. and Kandhasamy, R., 2016. Effect of Heat Input on Mechanical and Metallurgical Properties of Gas Tungsten Arc Welded Lean Super Martensitic Stainless Steel. *Materials Research*, 19(3), pp.572-579.
- Oliwa, R., 2015. Aramis application for measuring of three-dimensional local strain of composites. *Mechanik*, (12), pp.975/147-975/151.
- Pirinen, M., Martikainen, Y., Layus, P., Karkhin, V. and Ivanov, S., 2015. Effect of heat input on the mechanical properties of welded joints in high-strength steels. *Welding International*, 30(2), pp.129-132.
- Rasche, C. and Kuhlmann, U., 2009. Investigations on longitudinal fillet welded lap joints of HSS. *Nordic steel construction conference*, pp. 3-12.
- Sefcikova, K., Brtnik, T., Dolejs, J., Keltamaki, K. and Topilla, R., 2015. Mechanical Properties of Heat Affected Zone of High Strength Steels. *IOP Conference Series: Materials Science and Engineering*, 96, p.012053.

SFS-EN ISO 15614-1:2017, 2017. Specification and qualification of welding procedures for metallic materials. Welding procedure test. Part 1: Arc and gas welding of steels and arc welding of nickel and nickel alloys, pp.12-19.

Sarkkinen, J., 2021. Gleeble 3800 thermomechanical simulator. [online] Oulu.fi. Available at: <<https://www.oulu.fi/materialsengineering/gleeble3800>> [Accessed 12 September 2021].

Scholting, M. and Weber, B., 2007. Fatigue guidelines for thin high strength steel joint structures. Luxembourg: Off. for Official Publ. of the European Communities, pp.128-130.

Shamsuri, A. and Darus, S., 2020. Statistical Analysis of Tensile Strength and Flexural Strength Data from Universal Testing Machine. Asian Journal of Probability and Statistics, pp.54-62.

Singh, R., 2012. Applied welding engineering. Amsterdam [etc.]: Butterworth-Heinemann/Elsevier, pp.47-49.

Stier, B. and Reese, S., 2011. Verification of an optical metrology system (ARAMIS) by comparing experimental data with FE calculations and continuum approaches. PAMM, 11(1), pp.289-290.

SSAB. 2021. The high-strength structural steel with excellent formability. [online] Available at: <<https://www.ssab.com/products/brands/strenx/products/strenx-700-mc-plus>> [Accessed 15 September 2021].

Walotek, K., Bzówka, J. and Ciołczyk, A., 2021. Examples of the Use of the ARAMIS 3D Measurement System for the Susceptibility to Deformation Tests for the Selected Mixtures of Coal Mining Wastes. Sensors, 21(13), p.4600.

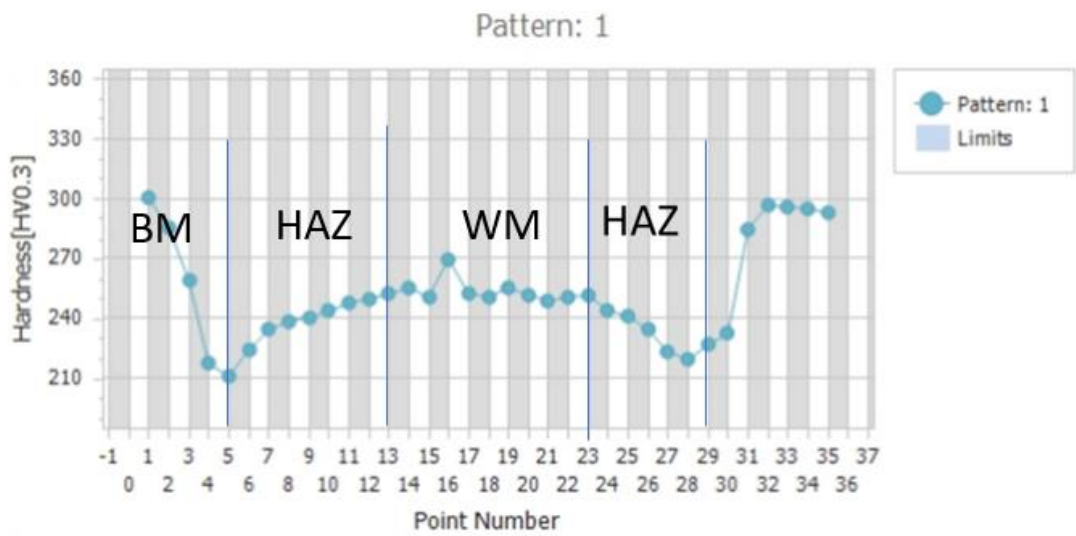
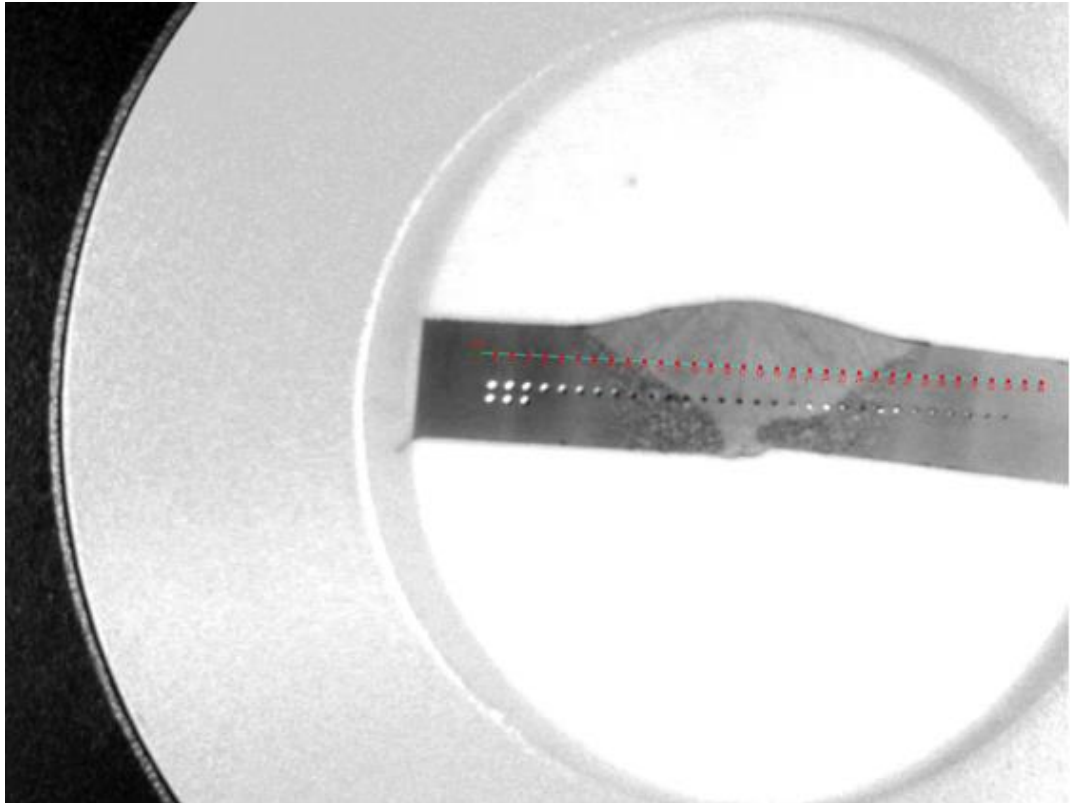
Yasuyama, M., Uchihara, M. and Fukui, K., 2007. Tailored blank technology of high strength steel sheet. Welding International, 21(4), pp.251-254.

Younise, B., 2014. Micromechanical fracture analysis of high strength steel weldments doctoral thesis. University of Belgrade, p.5.

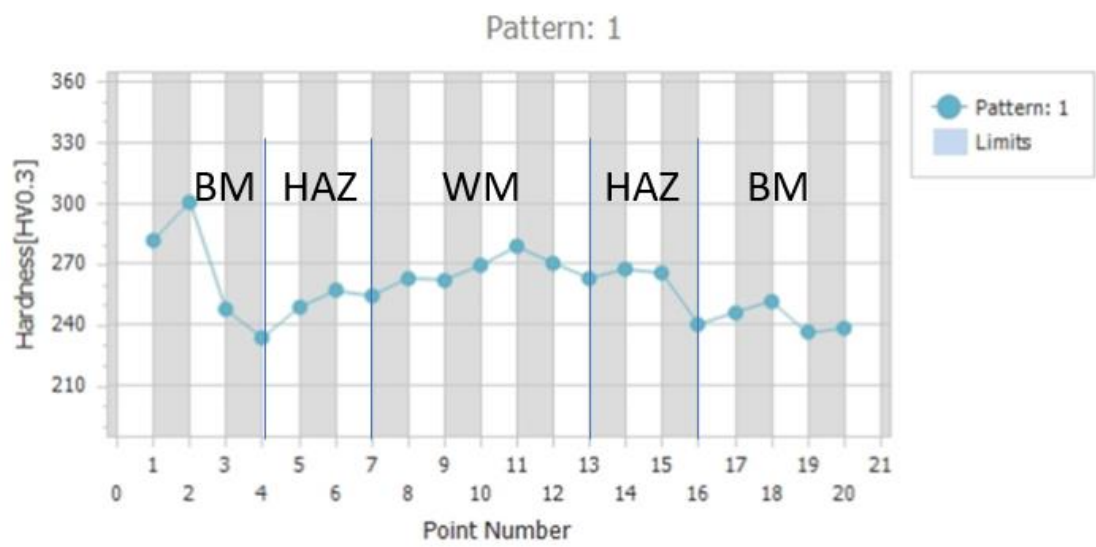


## APPENDICES

### APPENDIX 1: Hardness test profile

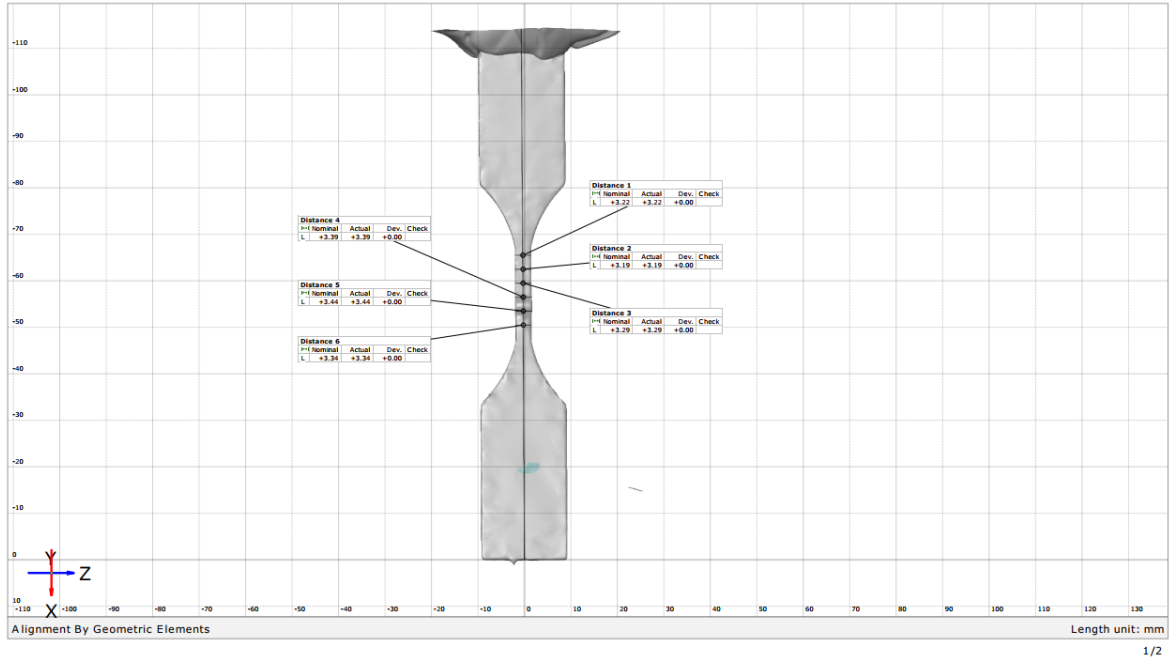


Hardness profile (High HI)

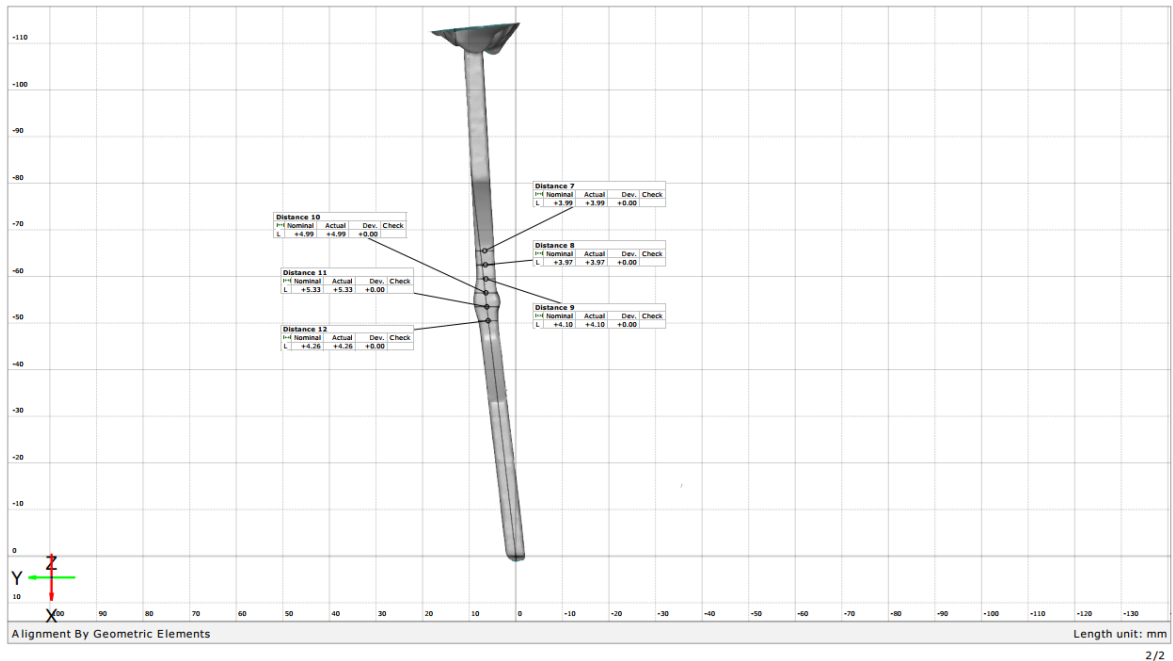


Hardness profile (Low HI)

APPENDIX 2: 3D scan data

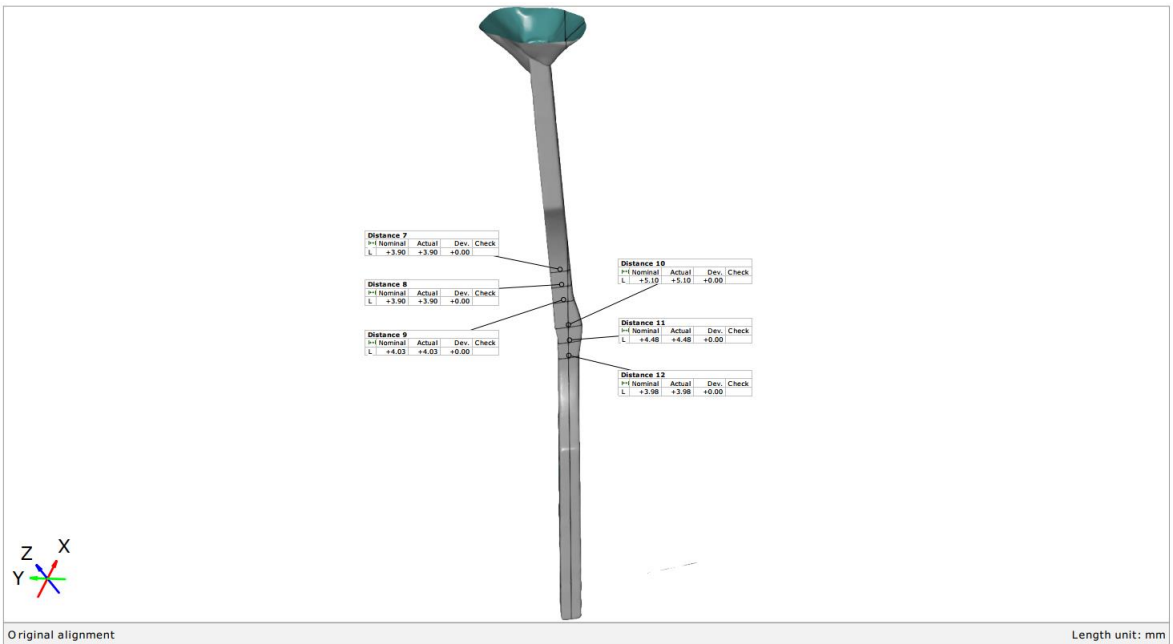
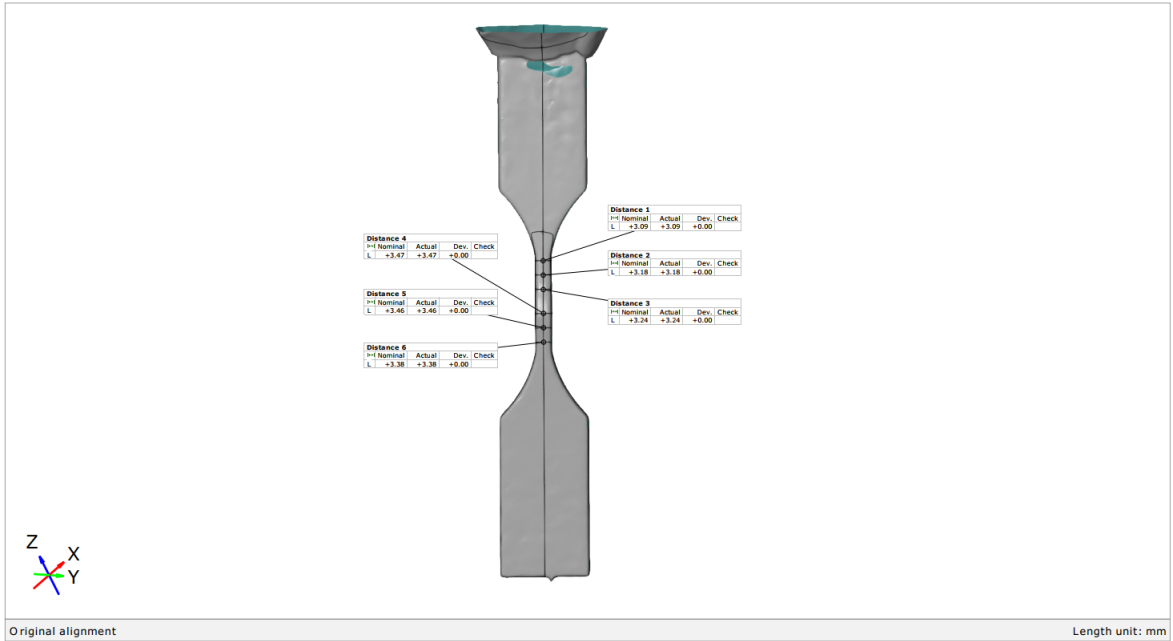


1/2

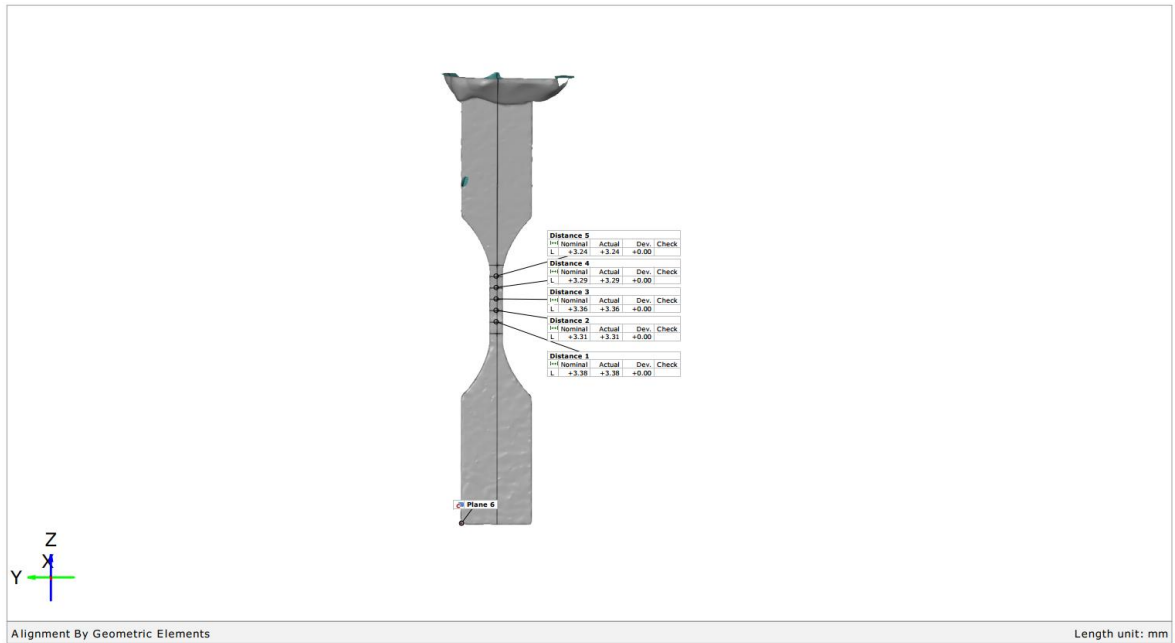


2/2

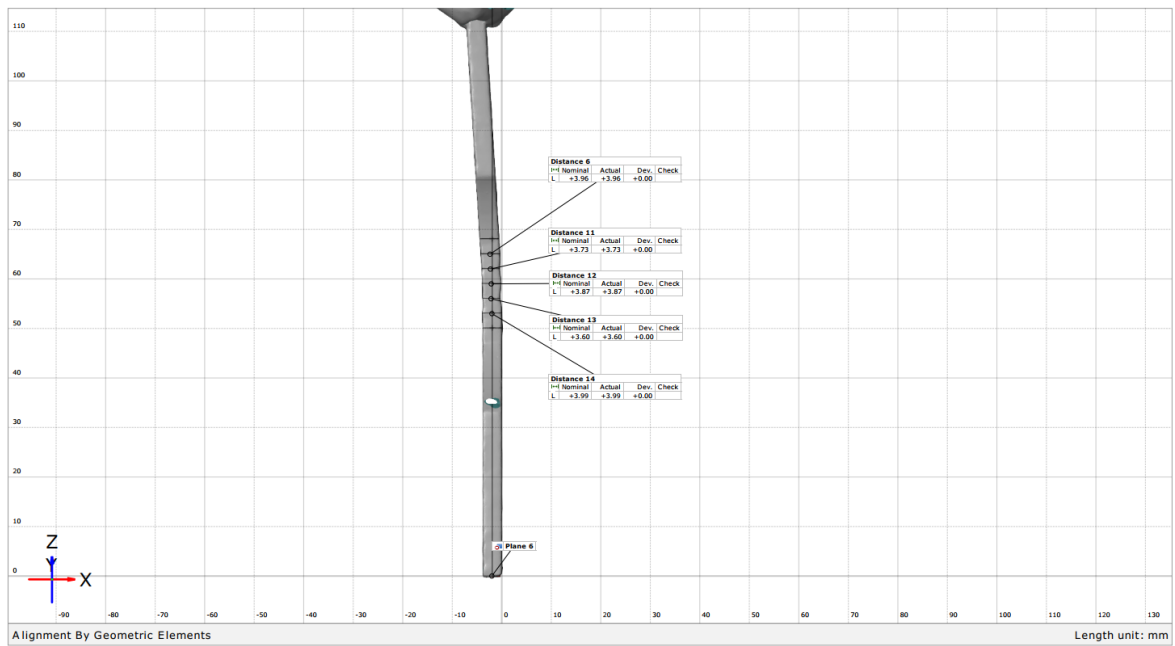
3D scan data for measuring cross section (SS1-High HI)



3D scan data for measuring cross section (SS2-High HI)

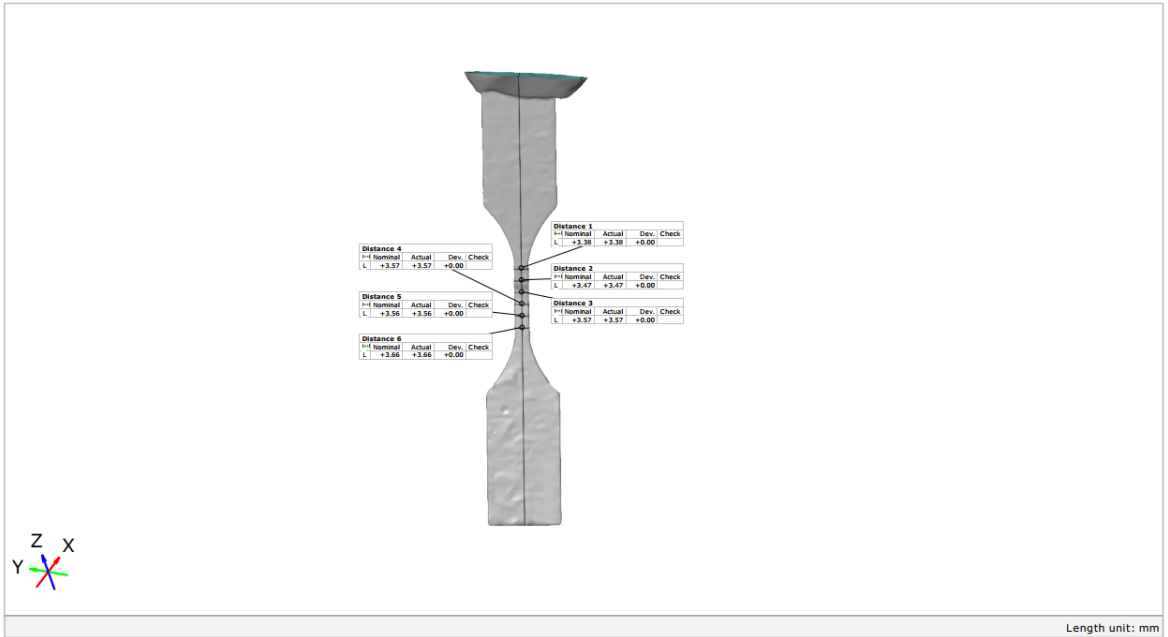


1/2

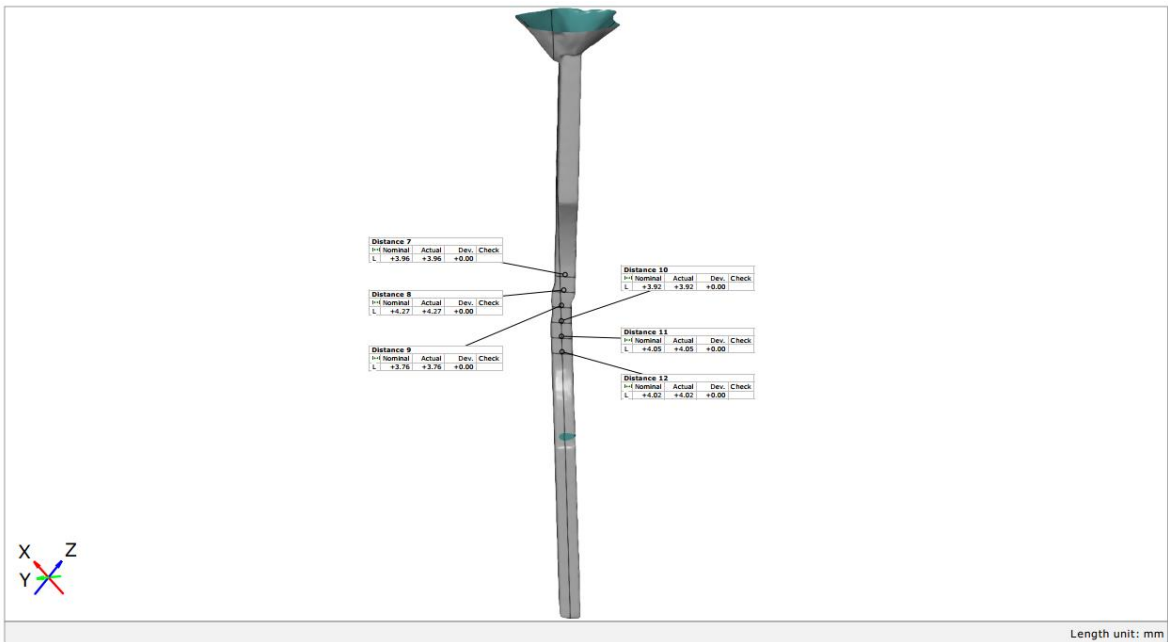


2/2

3D scan data for measuring cross section (SS1-Low HI)

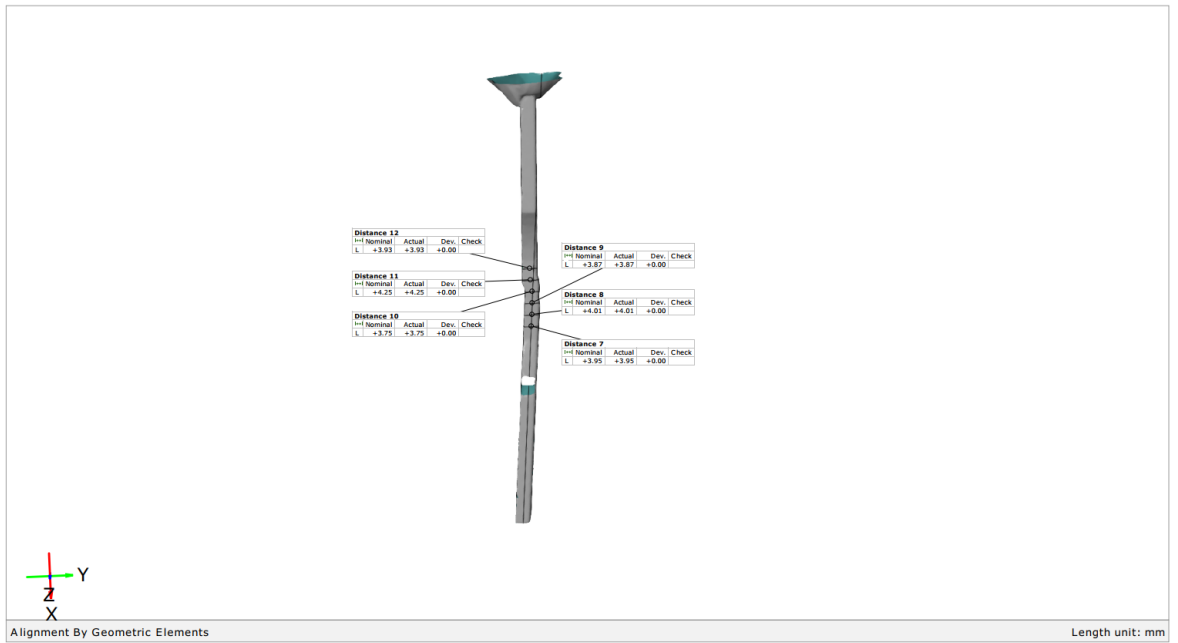
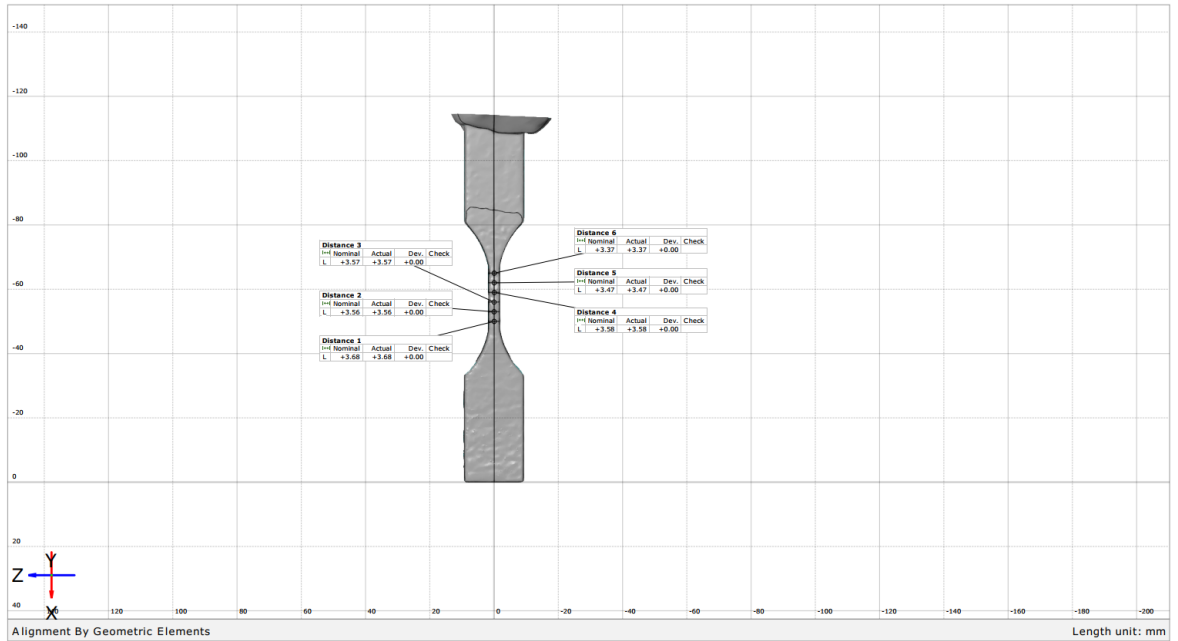


1/2

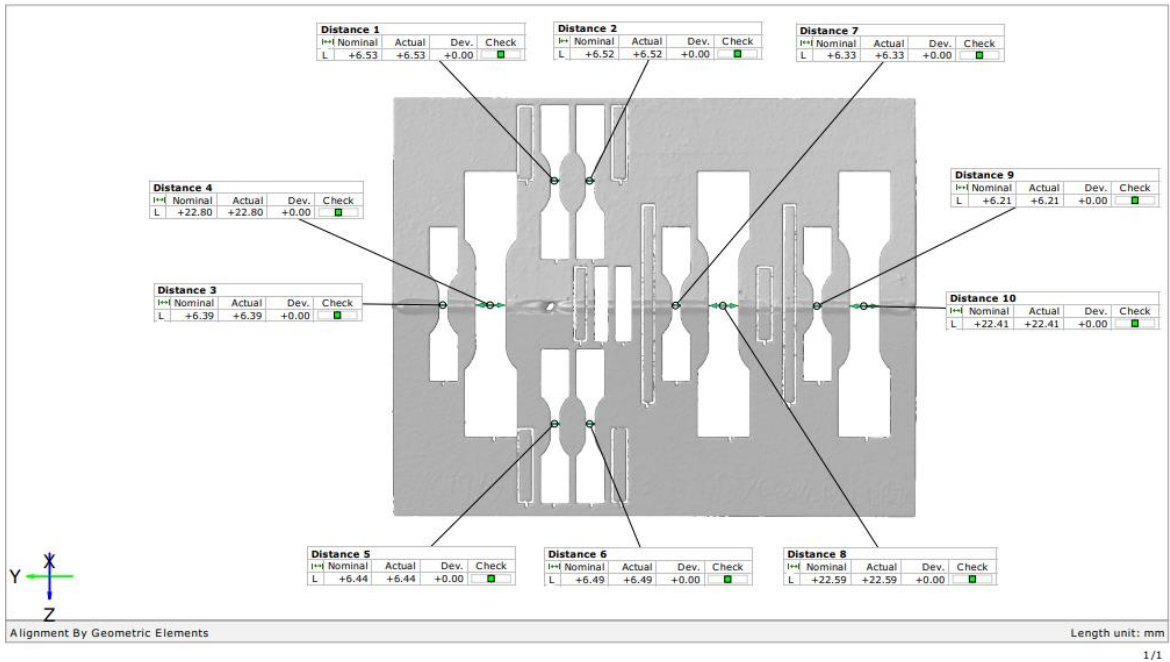


2/2

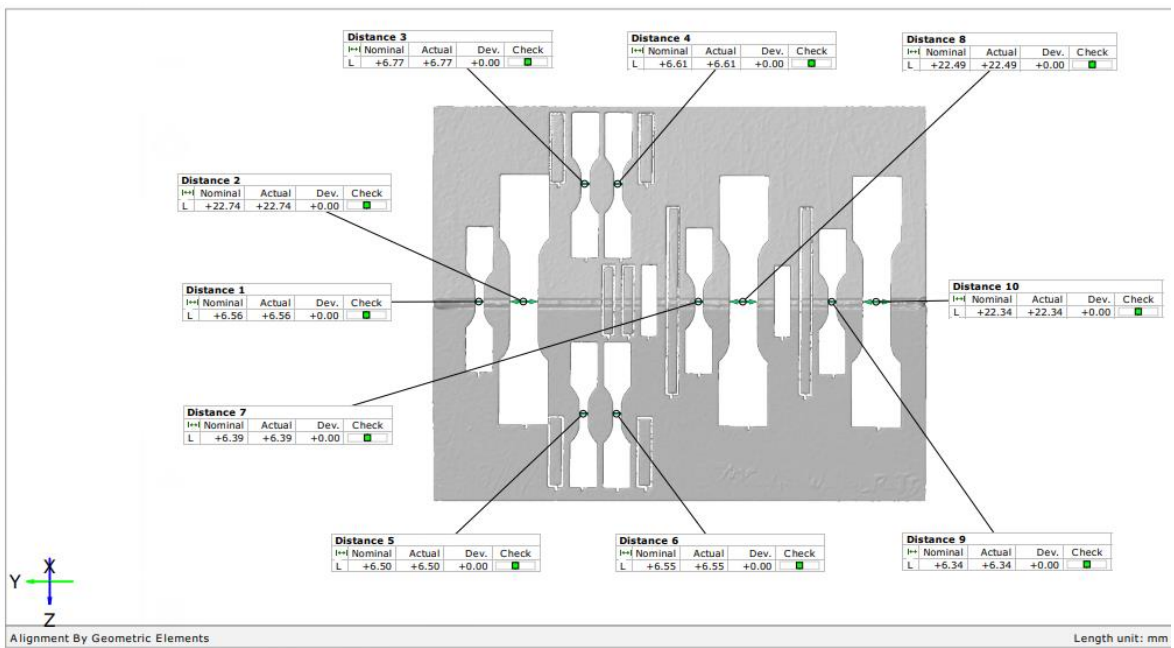
3D scan data for measuring cross section (SS2-Low HI)



3D scan data for measuring cross section (SS3-Low HI)



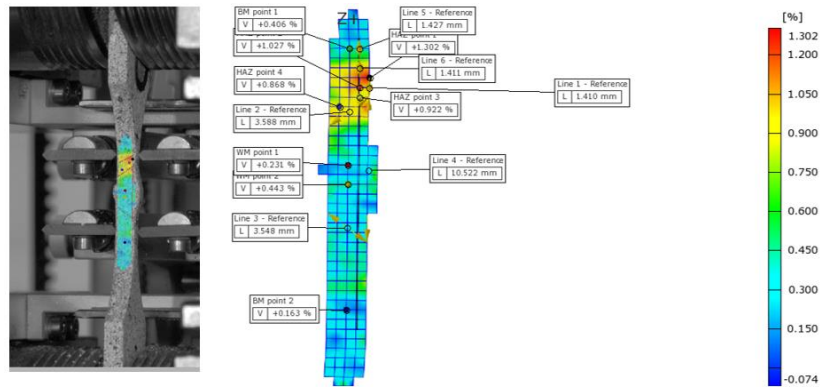
Water cut high HI large plate 3D scan.



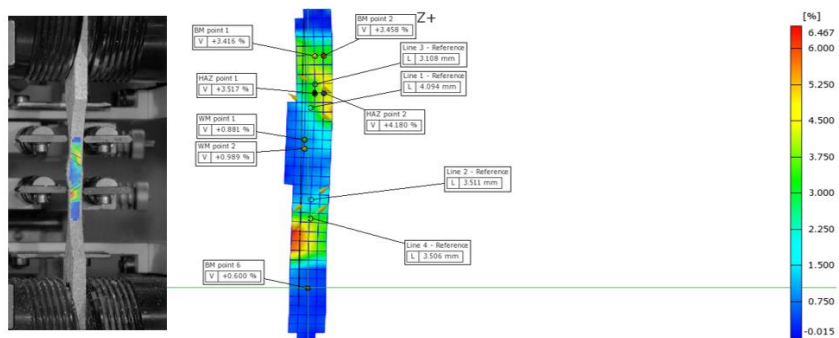
Water cut low HI large plate 3D scan.



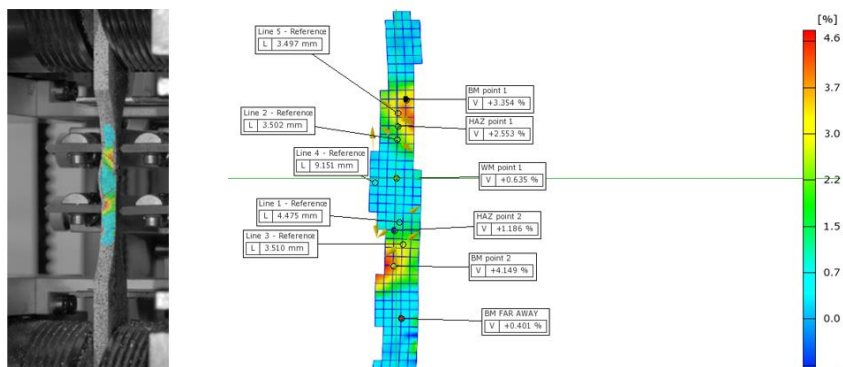
APPENDIX 3: Major strain at different load stage



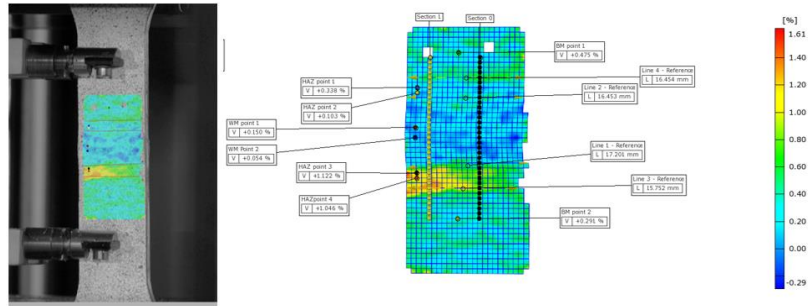
SS1-High HI. Major strain at the stage of (Standard Force 557.75 MPa)



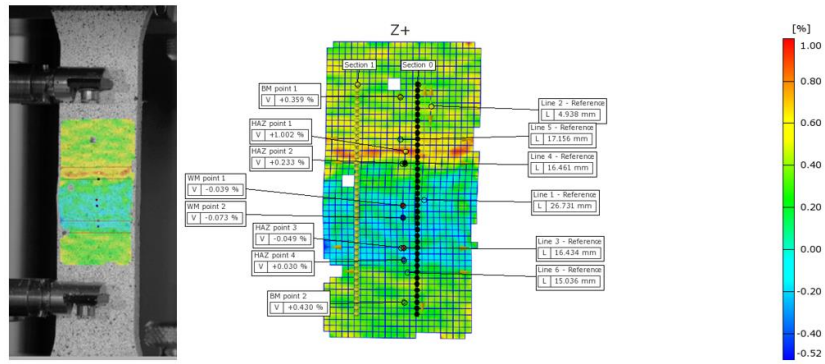
SS2-High HI. Major strain at the stage of (Standard Force 580.22 MPa)



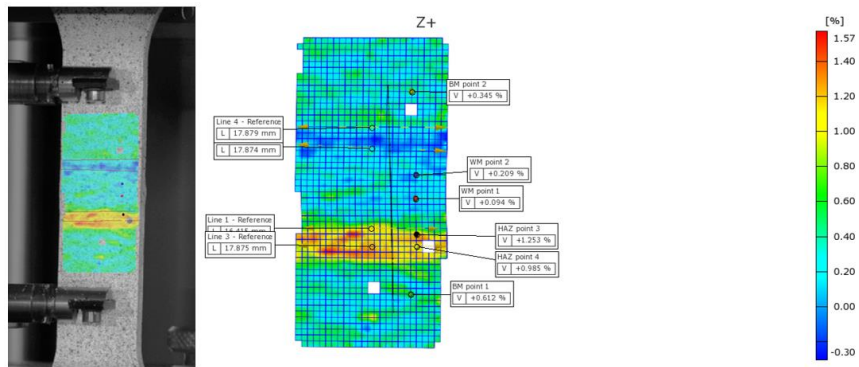
SS3-High HI. Major strain at the stage of (Standard Force 556.94 MPa)



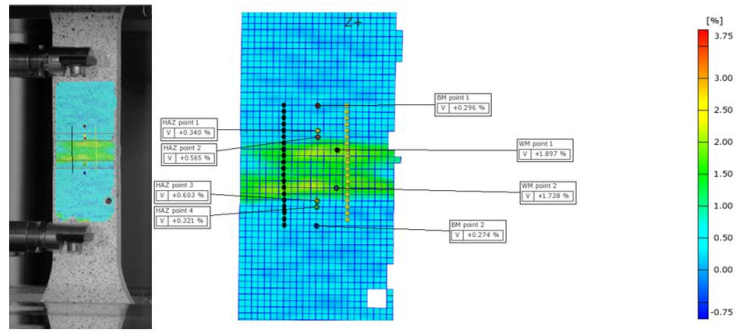
LS1-High HI. Major strain at the stage of (Standard Force 590.75 MPa)



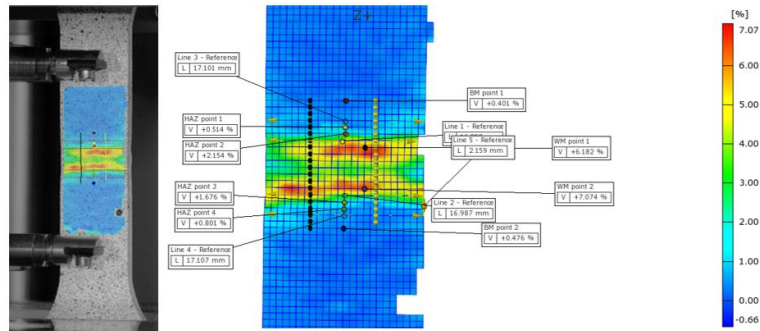
LS2-High HI. Major strain at the stage of (Standard Force 562.73 MPa)



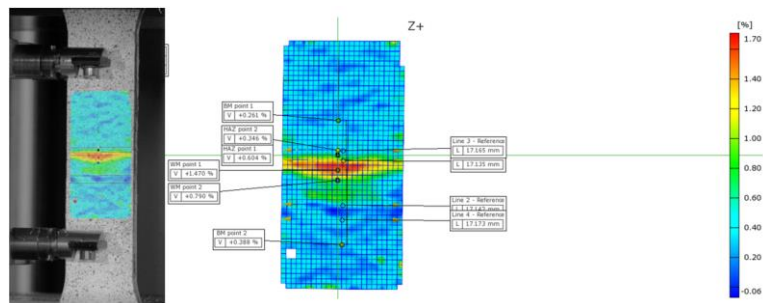
LS3- High HI. Major strain at the stage of (Standard Force 600.62 MPa)



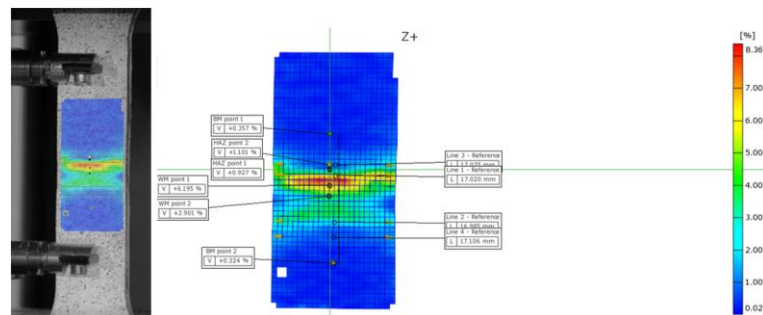
LS1-High HI. Major strain at the stage of (Standard Force 621.46 MPa)



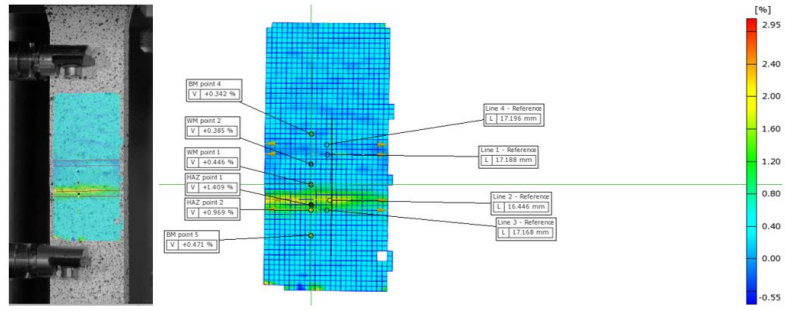
LS1-High HI. Major strain at the stage of (Standard Force 683.71 MPa)



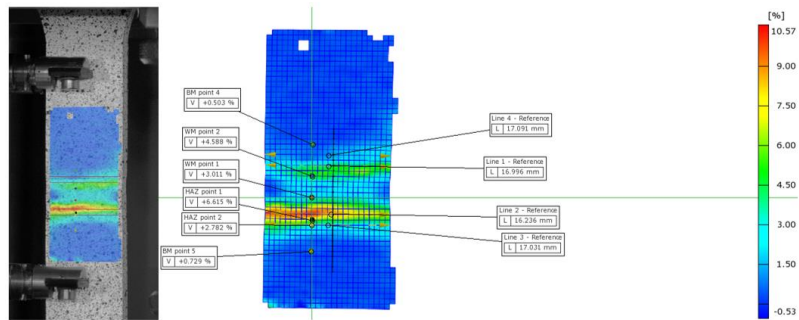
LS2-High HI. Major strain at the stage of (Standard Force 626.40 MPa)



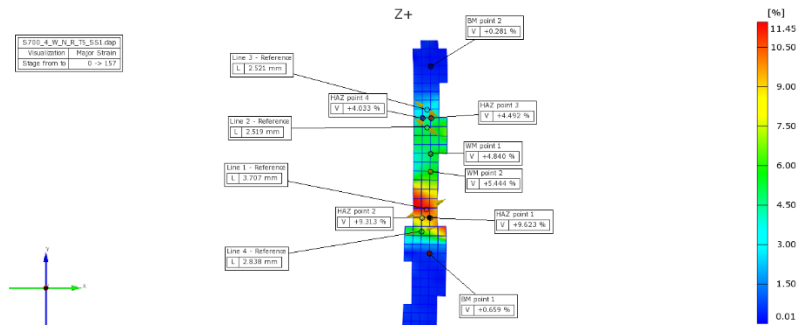
LS2-High HI. Major strain at the stage of (Standard Force 701.64 MPa)



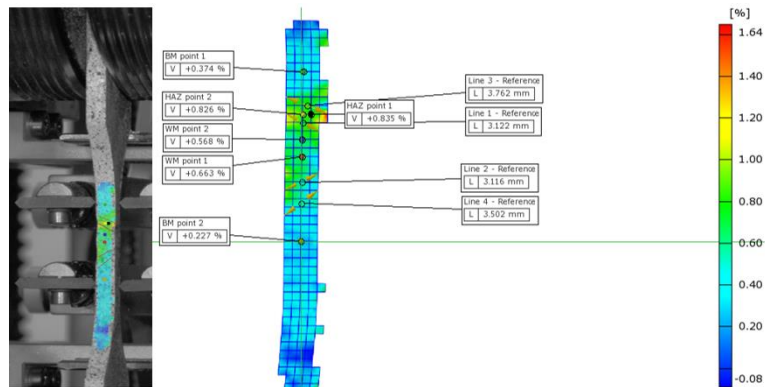
LS3-High HI. Major strain at the stage of (Standard Force 635.02 MPa)



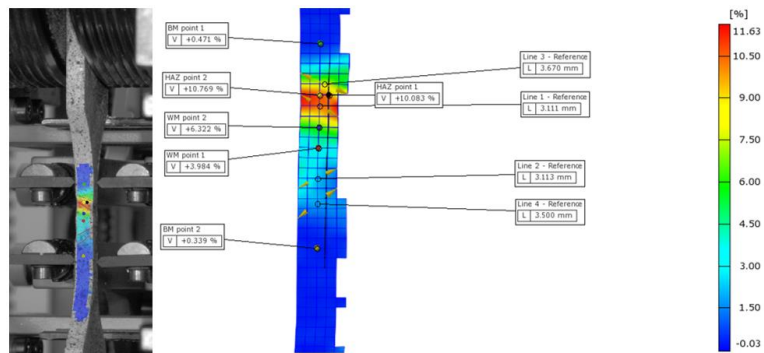
LS3-High HI. Major strain at the stage of (Standard Force 733.38 MPa)



SS1-Low HI. Major strain at the stage of (Standard Force 598.92 MPa)



SS2-Low HI. Major strain at the stage of (Standard Force 593,15 MPa)



SS2-Low HI. Major strain at the stage of (Standard Force 614.59 MPa)